

Model-Based Calibration of Transmission Test Bench Controls for Hardware-in-the-Loop Applications

Original

Model-Based Calibration of Transmission Test Bench Controls for Hardware-in-the-Loop Applications / Galvagno, E.; Tota, A.; Mari, G.; Velardocchia, M. (MECHANISMS AND MACHINE SCIENCE). - In: Advances in Engine and Powertrain Research and Technology / Parikyan T.. - STAMPA. - Cham : Springer Science and Business Media B.V., 2022. - ISBN 978-3-030-91868-2. - pp. 309-341 [10.1007/978-3-030-91869-9_13]

Availability:

This version is available at: 11583/2961513 since: 2022-04-15T13:20:06Z

Publisher:

Springer Science and Business Media B.V.

Published

DOI:10.1007/978-3-030-91869-9_13

Terms of use:

This article is made available under terms and conditions as specified in the corresponding bibliographic description in the repository

Publisher copyright

Springer postprint/Author's Accepted Manuscript (book chapters)

This is a post-peer-review, pre-copyedit version of a book chapter published in Advances in Engine and Powertrain Research and Technology. The final authenticated version is available online at: http://dx.doi.org/10.1007/978-3-030-91869-9_13

(Article begins on next page)

Metadata of the chapter that will be visualized in SpringerLink

Book Title	Advances in Engine and Powertrain Research and Technology	
Series Title		
Chapter Title	Model-Based Calibration of Transmission Test Bench Controls for Hardware-in-the-Loop Applications	
Copyright Year	2022	
Copyright HolderName	The Author(s), under exclusive license to Springer Nature Switzerland AG	
Corresponding Author	Family Name	Galvagno
	Particle	
	Given Name	Enrico
	Prefix	
	Suffix	
	Role	
	Division	
	Organization	Politecnico Di Torino
	Address	10129, Turin, Italy
	Email	enrico.galvagno@polito.it
	ORCID	https://orcid.org/0000-0003-2558-8798
Author	Family Name	Tota
	Particle	
	Given Name	Antonio
	Prefix	
	Suffix	
	Role	
	Division	
	Organization	Politecnico Di Torino
	Address	10129, Turin, Italy
	Email	antonio.tota@polito.it
	ORCID	https://orcid.org/0000-0002-7151-8873
Author	Family Name	Mari
	Particle	
	Given Name	Gianluca
	Prefix	
	Suffix	
	Role	
	Division	
	Organization	Politecnico Di Torino
	Address	10129, Turin, Italy
	Email	gianluca.mari@polito.it
Author	Family Name	Velardocchia
	Particle	
	Given Name	Mauro

Prefix
Suffix
Role
Division
Organization Politecnico Di Torino
Address 10129, Turin, Italy
Email mauro.velardocchia@polito.it
ORCID <https://orcid.org/0000-0003-0757-1626>

Abstract

Hardware in the loop test rigs represent one of the most adopted experimental platforms to assess automotive transmissions dynamic performances. Even if their architectures may range among few different configurations, they share general requirements from the mechanical design to their controller implementation for a real-time deployment. This chapter is focused on a real application of a Dual Clutch Transmission Hardware in the Loop test rig. Two electric motors are installed to emulate the effect of the Internal Combustion Engine to the transmission input and the vehicle motion resistances to the transmission output, respectively. For a proper Hardware in the Loop operation, if a torque control is selected for one electric motor, the second one requires to be controlled in speed. Moreover, the controls structure cannot be usually customized since they are conventionally constrained by industrial drive limitations. This chapter includes an accurate analysis of the reciprocal influence of the two controllers since they are mechanically applied to the input and output of the same transmission. The analysis is further supported by a linear model of the transmission test rig which is able to predict the sensitivity effect of the two controller's activation on the test rig performance. An optimal tuning of the two controllers' parameters is then described to achieve the desired level of reference tracking and disturbance rejection targets.

Keywords
(separated by '-')

Dynamic modelling - HiL testing - Experimental model validation - Transmission test bench - Control calibration - Frequency response functions - AC motors speed and torque control tuning - Torsional vibrations

Model-Based Calibration of Transmission Test Bench Controls for Hardware-in-the-Loop Applications



Enrico Galvagno , Antonio Tota , Gianluca Mari,
and Mauro Velardocchia 

1 **Abstract** Hardware in the loop test rigs represent one of the most adopted experi-
2 mental platforms to assess automotive transmissions dynamic performances. Even if
3 their architectures may range among few different configurations, they share general
4 requirements from the mechanical design to their controller implementation for a
5 real-time deployment. This chapter is focused on a real application of a Dual Clutch
6 Transmission Hardware in the Loop test rig. Two electric motors are installed to
7 emulate the effect of the Internal Combustion Engine to the transmission input and
8 the vehicle motion resistances to the transmission output, respectively. For a proper
9 Hardware in the Loop operation, if a torque control is selected for one electric motor,
10 the second one requires to be controlled in speed. Moreover, the controls structure
11 cannot be usually customized since they are conventionally constrained by indus-
12 trial drive limitations. This chapter includes an accurate analysis of the reciprocal
13 influence of the two controllers since they are mechanically applied to the input and
14 output of the same transmission. The analysis is further supported by a linear model
15 of the transmission test rig which is able to predict the sensitivity effect of the two
16 controller's activation on the test rig performance. An optimal tuning of the two
17 controllers' parameters is then described to achieve the desired level of reference
18 tracking and disturbance rejection targets.

19 **Keywords** Dynamic modelling · HiL testing · Experimental model validation ·
20 Transmission test bench · Control calibration · Frequency response functions · AC
21 motors speed and torque control tuning · Torsional vibrations

E. Galvagno (✉) · A. Tota · G. Mari · M. Velardocchia
Politecnico Di Torino, 10129 Turin, Italy
e-mail: enrico.galvagno@polito.it

A. Tota
e-mail: antonio.tota@polito.it

G. Mari
e-mail: gianluca.mari@polito.it

M. Velardocchia
e-mail: mauro.velardocchia@polito.it

© The Author(s), under exclusive license to Springer Nature Switzerland AG 2022
T. Parikyan (ed.), *Advances in Engine and Powertrain Research and Technology*,
Mechanisms and Machine Science 114,
https://doi.org/10.1007/978-3-030-91869-9_13

1

1 Introduction

Automotive transmission systems are designed to comply with strict functionality, reliability, and safety requirements to meet the desired vehicle drivability performance [1]. Usually, carmakers face the transmission development process through extensive experimental campaigns carried out to evaluate the transmission performance. A complete experimental set-up would require the connection of the transmission system to the internal combustion engine (ICE) or its direct installation on board the vehicle to reproduce with high fidelity the working operating conditions. However, this solution presents a considerable number of drawbacks in terms of costs and maintenance services that an ICE or a full vehicle system would implicate. Therefore, a more convenient solution involves the introduction of one or more electric motors to emulate the steady-state and the dynamic characteristics of the ICE as well as the load condition imposed by the vehicle motion resistances [2]. In this regard, Hardware-In-the-Loop (HiL) test benches have been very popular due to their advantages in terms of cost, flexibility, repeatability, and test automation since they adopt a model-based approach with a mix of real and emulated sensors, actuators, and vehicle subsystems to meet the cost and time constraints. HiL can reduce the testing effort up to a 90% if compared to the conventional driving test procedures, as described in [3]. Furthermore, HiL test benches have been widely used in the automotive industry to study the behavior of physical vehicle components and subsystems, e.g. the dual mass flywheel influence on transmission dynamics in [4], or to design and validate electronic control units. For example, a HiL simulation has been developed in [5, 6] for testing active brake control strategies such the Anti-lock Brake System (ABS), the Traction Control System (TCS), and the Electronic Stability Program (ESP). A similar application is also presented in [7–9], where a continuous braking pressure control strategy is implemented and validated on a HiL test rig with a conventional passenger car braking system. In [10] a HiL system is set-up for the development process of an electronic steering device to guarantee repetitive simulations and to demonstrate the efficacy with respect to on-board vehicle testing sessions. Finally, it is also convenient to integrate two or more HiL test rigs for evaluating their mutual influence, as also described by [11] where a DCT and a brake HiL systems are coupled to enhance the transmission Noise, Vibrations, Harshness (NVH) performance.

The activity described in this paper presents a real application of a DCT HiL test rig available at the Politecnico di Torino. Two electric motors are installed to emulate the effect of the ICE to the transmission input and the vehicle motion resistances to the transmission output, respectively. The control units of the electric motors adopted for HiL purposes, are usually designed with a rigid structure, typically a Proportional Integral Derivative (PID) logic, that is conventionally constrained by industrial drive limitations. The main contribution of the paper is to provide a model-based approach for analyzing and tuning the interaction between the control of the two electric motors. The torsional dynamics of the driveline installed on the test bench is simulated through a 6-degree-of-freedom (DOF) lumped parameter model, that represents an extended version of the 5-DOF model proposed in [12]. The transmission model

65 is also enhanced by considering the closed-loop dynamics introduced by the PID
66 algorithm for regulating the speed of one electric motor. An extensive sensitivity
67 analysis of the model to the mechanical and control parameters is proposed to evalu-
68 ate their effect on the controller reference speed tracking performance and on its
69 disturbance rejection against the torque applied by the second electric motor. Then,
70 the tuned speed control strategy is experimentally validated on the DCT HiL test rig.

71 The manuscript is organized as follows: Sect. 2 provides an overview of the
72 hardware and software available on the DCT HiL test rig; Sect. 3 introduces the
73 transmission model, and analyze the dynamic behavior of both open-loop and closed-
74 loop configurations; Sect. 4 presents the sensitivity analysis of the linear model
75 to the mechanical and control parameters, while Sect. 5 covers the experimental
76 validation, both in frequency and time domain, of the proposed methodology; finally,
77 conclusions are drawn in Sect. 6.

78 2 Transmission HiL Test Rig: Hardware (HW) 79 and Software (SW)

80 The test bench here presented is meant to be used as a HiL system for automotive
81 transmission testing. The typical loading condition associated with the usage of a
82 mechanical transmission on a real car can be reproduced. To this aim, a simulation
83 model running and exchanging in real time signals with sensors and actuators is
84 implemented. Some examples of test benches sharing a similar HiL technology are
85 reported in [13, 14]. A detailed description of the hardware and software components
86 is given in the next two sections.

87 2.1 Hardware Components

88 Figure 1 shows a picture of the HiL transmission test bench in the Mechanical
89 Laboratory of Politecnico di Torino. It features two electric motors (M1 and M2)
90 and two transmissions, the first is a Dual Clutch Transmission (DCT), that is the
91 system under investigation, and the second a Manual Transmission (MT).

92 As visible in Fig. 2, the connection between the two transmissions is realized
93 through the two output shafts SA1 and SA2, i.e. the original left half shafts of the
94 two drivelines, and a brake disk D.

95 More specifically, the main subsystems that are visible in Fig. 1 are commented
96 below (starting from the left part of the picture):

- 97 (i) M1: a 37 kW 2-pole 3-phase induction motor featuring a nominal torque of
98 121 Nm and a nominal speed of 2920 rpm. It is operated in the four quadrants
99 of the torque-speed plane by an inverter with a torque overload capacity of
100 150%. For this application, the “torque-control with speed limitation” mode



Fig. 1 Transmission test bench in the Mechanical Laboratory of Politecnico di Torino

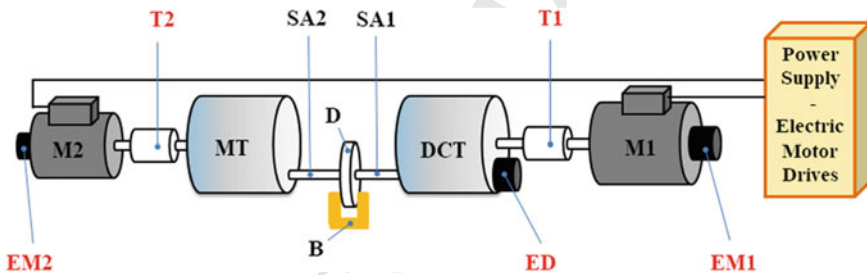


Fig. 2 Layout of the transmission test bench: electric motors (M1, M2), speed sensors (encoders EM1, EM2 and ED), torque sensors (T1, T2), disk (D), brake (B) and half shafts (SA1, SA2)

is selected for reproducing the torque delivered by the internal combustion engine of the car.

- (ii) DCT: a 6-speed dry Dual Clutch Transmission (see, e.g., [15] for the kinematic and dynamic behavior of this transmission).
- (iii) MT: a 6-speed Manual Transmission with one primary and two secondary shafts;
- (iv) M2: a 11 kW 6-pole 3-phase induction motor with a nominal torque of 110 Nm and a nominal speed of 955 rpm. It is powered by an inverter with 150% torque overload capacity which allows the electric machine operating in four quadrants. For this application, the “encoder feedback speed-control” mode is selected and is used to simulate the vehicle load at the output shaft of the DCT, that is due to the aerodynamic and rolling resistance, the road slope, and the vehicle inertial effects.

To monitor the actual dynamic state of the transmission system, the test bench is equipped with a number of sensors that are here reported.

- (i) Two torque-meters (T1 and T2 in Fig. 2), measuring the torque provided by the two electric motors: T1 torque meter, is particularly suitable for dynamic torque measurements having a bandwidth of 3 kHz and a maximum torque of 500 Nm; T2 is a torque meter with an integrated tachometer, capable of withstanding dynamic torques of 226 Nm.
- (ii) Three rotary incremental encoders: EM1 and EM2 measure the angular position and speed of the two motors while ED measures the position and speed of the DCT differential; the number of pulses per revolution of the three sensors are 1024, 4096 and 9600 respectively. It is worth noting that encoders EM1 and EM2 are the same sensors used by the electric drives for implementing the closed-loop speed control of the two motors.
- (iii) Magnetic pickup sensors for monitoring the angular speed of the components inside the DCT, they are positioned: on the secondary mass of the dual mass flywheel, on the differential crown, on the two differential pinions (lower and upper secondary shaft), on the first and third gear on the lower secondary shaft and on the second and fourth gear on the upper secondary shaft.
- (iv) Two thermocouples are also mounted on the DCT, one for measuring the temperature of the lubricating oil and the other one for monitoring the temperature of the hydraulic fluid of the actuation system.
- (v) A triaxial accelerometer on the gearbox housing and a microphone for further NVH analysis, e.g. gearshift noise and vibration.

The two electric motors are operated by means of electric drives, the 37 and 11 kW inverters shown in Fig. 3, which allow controlling either the actual torque or the speed in open or closed-loop, the latter through PID controllers, depending on the user's choice. Both the drives are set for operating with vector control method.

The electric cabinet of the test rig also include an Active Front End (AFE) which connects the two inverters via a direct current (DC) bus, allowing an efficient power exchange between the two motor drives. AFE may absorb or give back to the electric grid the net electric power deriving from the specific operating condition of the bench. Power regeneration is therefore enabled through this system architecture,

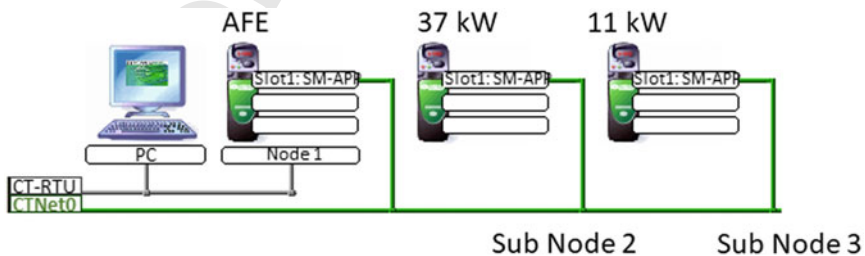


Fig. 3 Communication network between the electric drives (37 and 11 kW) and the active front end (AFE)

146 thus avoiding the dissipation, e.g. on braking resistors, the negative electric power.
 147 For closed-loop control, the microcontrollers inside the electrical cabinet use the
 148 information from the torque transducers and the encoders mounted on the bench.
 149 The front panel of the electrical cabinet features displays for manual settings of
 150 the motor drives and many connectors for analog and digital I/O, Controller Area
 151 Network (CAN) and Ethernet communication for real-time control of the test bench
 152 and for remote monitoring and programming the inverter parameters.

153 It is worth underlining that a good controllability of both electric motors in terms
 154 of torque and speed reference tracking performance is mandatory for such kind of
 155 test bench. The optimization of the available parameters, in particular the PID gains
 156 of the feedback controllers, is crucial for obtaining a satisfactory trade-off between
 157 the conflicting requirements, i.e. high dynamic performance, low control effort and
 158 low noise and vibrations. The step change of some system parameters during the
 159 normal working condition of the bench, i.e. the gear ratio of the two transmissions,
 160 leads to different optimal parameter sets for different test bench configurations. This
 161 last specific characteristic requires specific analysis and considerations that are the
 162 aim of this paper.

163 2.2 Software Components

164 The HiL testing methodology requires modelling the dynamics of all the systems
 165 interacting with the transmission under test that are present on a real car, but that
 166 are not physically installed on the bench. Figure 4 highlights the main interactions
 167 between hardware and software components of the test bench. In the central part
 168 of the picture are the two models for engine and vehicle simulation, on the left the
 169 inputs signals from the Transmission Control Unit (TCU) via CAN, from encoder
 170 and torque sensors, while on the right the output signals for the TCU, the torque and
 171 the speed setpoints for the controllers of the two motors.

172 Suitable models for the internal combustion engine and for the vehicle longitudinal
 173 dynamics simulation must be developed and implemented in the HiL software.

174 Vehicle dynamics model

175 A 1 degree of freedom model for the vehicle longitudinal dynamics is normally
 176 adequate for the present application, in which the pure rolling condition for the tires
 177 is assumed. The model must account for the motion resistance due to aerodynamics,
 178 rolling and road slope and for the inertial effects of the vehicle. This block computes
 179 the reference speed for M2 motor according to the torque applied by the powertrain
 180 and measured by T2 torque sensors and the actual speed of M2 motor.

181 Engine model

182 The engine model must include the following functions to accomplish the tasks
 183 required by HiL transmission testing for conventional powertrains: starter simulation,
 184 engine cut-off during accelerator pedal release, redline control for maximum speed

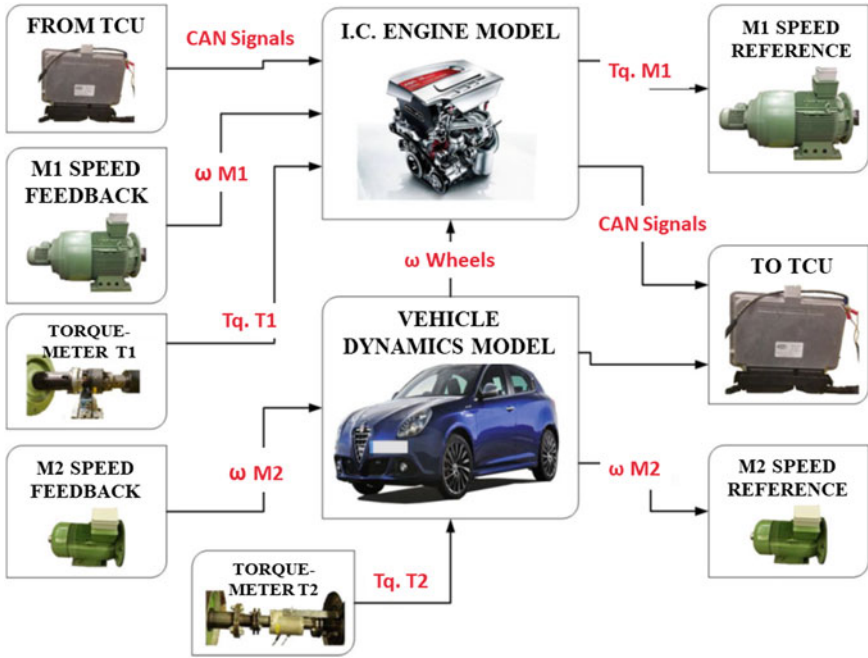


Fig. 4 HiL software scheme: on the left) the inputs from the TCU and the torque and speed sensors of the electric motors, in the middle) the main simulation blocks, on the right) the output setpoints for the electric motors and the signals for the TCU

185 limitation, idle speed control, torque saturation according to engine maximum and
 186 minimum torque map, combustion delay and turbo lag to account for the delay
 187 introduced by the gasoline or diesel engine torque generation system. Figure 5 shows
 188 a block diagram of the engine model, in which the said functions are reported; this
 189 model computes the torque delivered by the virtual ICE according to the actual
 190 working condition of the bench. The engine torque signal becomes a reference for
 191 the torque control of M1 motor and is sent via CAN to the corresponding drive.

192 Typical examples of experiments carried out on the test bench include: vehicle
 193 start-up, gear shift, engine start and stop, accelerator pedal tip-in/tip-out, run-up
 194 and coast-down, acceleration and deceleration with upshifts and downshifts. This
 195 test bench was also recently used to study the integration with other active chassis
 196 systems with the aim of enhancing the transmission NVH performance.

197 3 System Model and Analysis

198 The DCT torsional dynamics is investigated through a six-degree-of-freedom (DOF)
 199 lumped parameter model, as shown in Fig. 6.

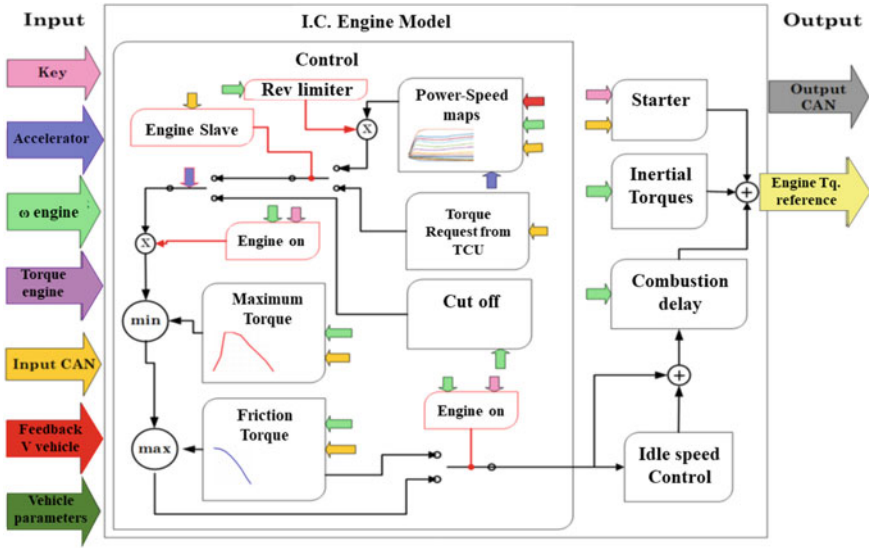


Fig. 5 ICE model block diagram. The colours of the arrow are used to identify which input enters in each single blocks from the central part of the picture

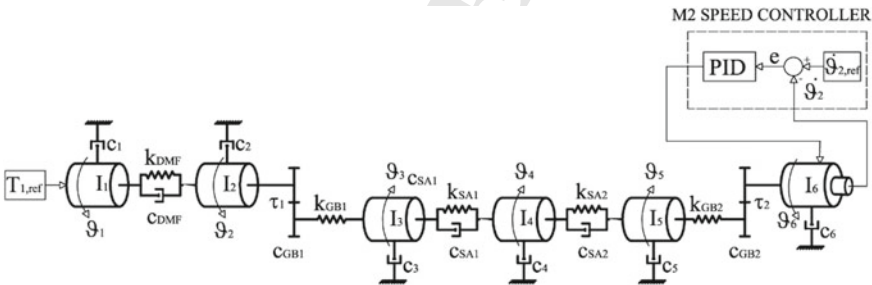


Fig. 6 Schematic of the torsional model of the transmission test bench

200

The test bench torsional model includes the following elements:

201

- The Dual Mass Flywheel (DMF) is modelled with two inertial components, I_1 and I_2 , linked by a low stiffness spring k_{DMF} and a viscous damper with damping coefficient c_{DMF} . The moment of inertia I_1 includes the first DMF mass and the M1 motor inertia, meanwhile the second DMF mass and the equivalent inertia of the DCT gearbox (except its differential inertia I_3) are integrated in I_2 .

202

203

204

205

206

207

208

209

210

- The DCT gearbox model account for the actual gear ratio τ_1 (defined as the ratio between the input and output speeds) and an equivalent torsional stiffness k_{GB1} at the transmission output shaft. The value of k_{GB1} varies with the gear ratio τ_1 due to the variation of the portion of the shaft through which the power is transmitted when the different gears are engaged.

- The MT gearbox is modelled with the actual gear ratio τ_2 and an equivalent stiffness k_{GB2} (evaluated at its output shaft) between differential inertia I_5 and inertia I_6 which includes the M2 mass moment of inertia and the equivalent inertia of the MT gearbox.
- The inertia of the brake disk I_4 connecting the DCT and MT output shafts through the two half shafts SA1 and SA2, respectively, which are modelled as a pair of spring damper elements.

The values of the said parameters used to define the transmission test bench model are reported in Table 1. While inertial and elastic parameters can be quite accurately derived from component technical drawing or data sheet, damping cannot be easily evaluated; therefore a curve fitting method based on the comparison of the simulated and experimental frequency response functions (FRFs) (see Sect. 3.3 for further information) was set up to identify the viscous damping parameters of the model.

As already mentioned in the former section, the electric motor M1 is usually set to apply a desired torque to emulate the steady-state torsional behavior of the ICE engine meanwhile the motor M2 is controlled in speed to replicate the vehicle longitudinal dynamics through the mathematical model of the motion resistance.

The system analysis is conducted in two steps that will be called.

- open-loop system* if the two motors M1 and M2 apply torque to the mechanical system without using any feedback signals from the test rig.
- closed-loop system* if M2 is speed controlled using feedback from EM1 sensor and M1 applies torque to the mechanical system without feedback.

3.1 Open-Loop System Equations

The equations of motion of the torsional model depicted in Fig. 6 are:

$$\begin{aligned}
 I_1 \ddot{\vartheta}_1 + c_{DMF}(\dot{\vartheta}_1 - \dot{\vartheta}_2) + c_1 \dot{\vartheta}_1 + k_{DMF}(\vartheta_1 - \vartheta_2) &= T_1 \\
 I_2 \ddot{\vartheta}_2 + \left(c_2 + \frac{c_{GB1}}{\tau_1^2} \right) \dot{\vartheta}_2 - c_{DMF}(\dot{\vartheta}_1 - \dot{\vartheta}_2) - \frac{k_{GB1}}{\tau_1} \left(\vartheta_3 - \frac{\vartheta_2}{\tau_1} \right) - k_{DMF}(\vartheta_1 - \vartheta_2) &= 0 \\
 I_3 \ddot{\vartheta}_3 + c_3 \dot{\vartheta}_3 + c_{SA1}(\dot{\vartheta}_3 - \dot{\vartheta}_4) + k_{GB1} \left(\vartheta_3 - \frac{\vartheta_2}{\tau_1} \right) + k_{SA1}(\vartheta_3 - \vartheta_4) &= 0 \\
 I_4 \ddot{\vartheta}_4 + c_4 \dot{\vartheta}_4 + c_{SA1}(\dot{\vartheta}_4 - \dot{\vartheta}_3) + c_{SA2}(\dot{\vartheta}_4 - \dot{\vartheta}_5) + k_{SA1}(\vartheta_4 - \vartheta_3) + k_{SA2}(\vartheta_4 - \vartheta_5) &= 0 \\
 I_5 \ddot{\vartheta}_5 + c_5 \dot{\vartheta}_5 + c_{SA2}(\dot{\vartheta}_5 - \dot{\vartheta}_4) + k_{GB2} \left(\vartheta_5 - \frac{\vartheta_6}{\tau_2} \right) + k_{SA2}(\vartheta_5 - \vartheta_4) &= 0 \\
 I_6 \ddot{\vartheta}_6 + \left(c_6 + \frac{c_{GB2}}{\tau_2^2} \right) \dot{\vartheta}_6 - \frac{k_{GB2}}{\tau_2} \left(\vartheta_5 - \frac{\vartheta_6}{\tau_2} \right) &= T_6 \quad (1)
 \end{aligned}$$

where $\tau_1 = \tau_{G1}\tau_{F1}$, $\tau_2 = \tau_{G2}\tau_{F2}$ and the generalized coordinates are the angular positions of each inertial component in Fig. 6: $\mathbf{q} = \{\vartheta_1 \vartheta_2 \vartheta_3 \vartheta_4 \vartheta_5 \vartheta_6\}^T$, and T_1 and T_6 represent the torques applied by M1 and M2, respectively.

Table 1 Parameters of the transmission test bench model

Quantity	Symbol	Value	Units
Primary DMF inertia	I_1	0.195	kgm^2
Secondary DMF inertia	I_2	0.147	kgm^2
DCT inertia (at output shaft)	I_3	0.123	kgm^2
Brake disk inertia	I_4	0.18	kgm^2
MT differential inertia	I_5	0.172	kgm^2
MT and M2 inertia	I_6	0.069	kgm^2
DCT gear ratio	τ_{G1}	[4.15, 2.27, 1.43, 0.98, 0.76, 0.62, -4]	—
MT gear ratio	τ_{G2}	[4.17, 2.35, 1.46, 0.95, 0.69, 0.55, -4.08]	—
DCT final drive ratio	τ_{F1}	4.118	—
MT final drive ratio	τ_{F2}	4.222	—
Fly-wheel stiffness	k_{DMF}	458.4	Nm/rad
DCT stiffness	k_{GB1}	$[2.73, 7.84, 0.96, 3.78, 0.33, 1.82] \times 10^5$	Nm/rad
MT stiffness	k_{GB2}	1.34×10^5	Nm/rad
First driveshaft stiffness	k_{SA1}	0.12×10^5	Nm/rad
Second driveshaft stiffness	k_{SA2}	0.15×10^5	Nm/rad
DOF damping	$[c_1, c_2, \dots, c_6]$	[0.2, 2, 0.02, 0.34, 4, 0]	Nms/rad
DMF Damping	c_{DMF}	7.5	Nms/rad
DCT damping	c_{GB1}	0	Nms/rad
MT damping	c_{GB2}	4	Nms/rad
First driveshaft damping	c_{SA1}	0.1	Nms/rad
Second driveshaft damping	c_{SA2}	0.1	Nms/rad

245 Equation (1) can be expressed with the following matrix formulation:

$$246 \quad \mathbf{M}\ddot{\mathbf{q}} + \mathbf{C}\dot{\mathbf{q}} + \mathbf{K}\mathbf{q} = \underbrace{\begin{bmatrix} 1 & 0 \\ 0 & 0 \\ 0 & 0 \\ 0 & 0 \\ 0 & 0 \\ 0 & 1 \end{bmatrix}}_{\mathbf{E}} \begin{bmatrix} T_1 \\ T_6 \end{bmatrix} \quad (2)$$

248 where the mass matrix \mathbf{M} , the damping matrix \mathbf{C} and the stiffness matrix \mathbf{K} are
249 defined as:

$$250 \quad \mathbf{M} = \text{diag}(I_1, I_2, I_3, I_4, I_5, I_6)$$

$$\mathbf{C} = \begin{bmatrix} c_{DMF} + c_1 & -c_{DMF} & 0 & 0 & 0 & 0 \\ -c_{DMF} & c_{DMF} + c_2 + \frac{c_{GB1}}{\tau_1} & 0 & 0 & 0 & 0 \\ 0 & 0 & c_3 + c_{SA1} & -c_{SA1} & 0 & 0 \\ 0 & 0 & -c_{SA1} & c_{SA1} + c_4 + c_{SA2} & -c_{SA2} & 0 \\ 0 & 0 & 0 & -c_{SA2} & c_5 + c_{SA2} & 0 \\ 0 & 0 & 0 & 0 & 0 & c_6 + \frac{c_{GB2}}{\tau_2} \end{bmatrix}$$

$$251 \quad \mathbf{K} = \begin{bmatrix} k_{DMF} & -k_{DMF} & 0 & 0 & 0 & 0 \\ -k_{DMF} & k_{DMF} + \frac{k_{GB1}}{\tau_1} & -\frac{k_{GB1}}{\tau_1} & 0 & 0 & 0 \\ 0 & -\frac{k_{GB1}}{\tau_1} & k_{GB1} + k_{SA1} & -k_{SA1} & 0 & 0 \\ 0 & 0 & -k_{SA1} & k_{SA1} + k_{SA2} & -k_{SA2} & 0 \\ 0 & 0 & 0 & -k_{SA2} & k_{SA2} + k_{GB2} - \frac{k_{GB2}}{\tau_2} & -\frac{k_{GB2}}{\tau_2} \\ 0 & 0 & 0 & 0 & -\frac{k_{GB2}}{\tau_2} & \frac{k_{GB2}}{\tau_2} \end{bmatrix} \quad (3)$$

252 The system is then expressed with the state-space representation:

$$253 \quad \dot{\mathbf{x}} = \underbrace{\begin{bmatrix} \mathbf{0}_{6 \times 6} & \mathbf{I}_{6 \times 6} \\ -\mathbf{M}^{-1}\mathbf{K} & -\mathbf{M}^{-1}\mathbf{C} \end{bmatrix}}_{\mathbf{A}_{OL}} \mathbf{x} + \underbrace{\begin{bmatrix} \mathbf{0}_{6 \times 2} \\ -\mathbf{M}^{-1}\mathbf{E} \end{bmatrix}}_{\mathbf{B}_{OL}} \mathbf{u} \quad (4)$$

255 where $\mathbf{x} = \{\mathbf{q} \dot{\mathbf{q}}\}^T$ is the state vector and $\mathbf{u} = \{T_1 \ T_6\}^T$ is the input vector.

256 Modal Analysis

257 By solving the eigenvalue problem associated with the system in Eq. (4), the damped
258 natural frequency $\omega_{n,r}$, the damping ratio ζ_r , the amplitude and phase of the complex
259 eigenvector $\boldsymbol{\psi}_r$ associated to the r_{th} mode are computed and shown in Figs. 7 and
260 8 for different values of the MT gears g_2 . The eigenvectors are normalized so that

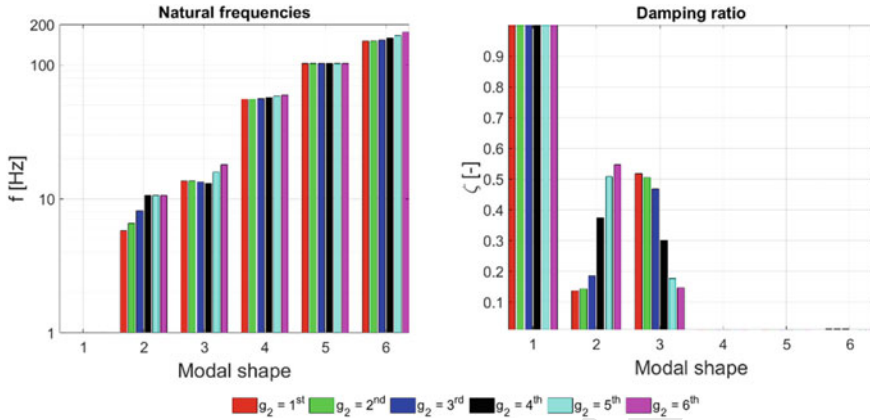


Fig. 7 Natural frequencies and damping ratio of the open-loop system with different MT gears and DCT gear $g_1 = 5^{th}$

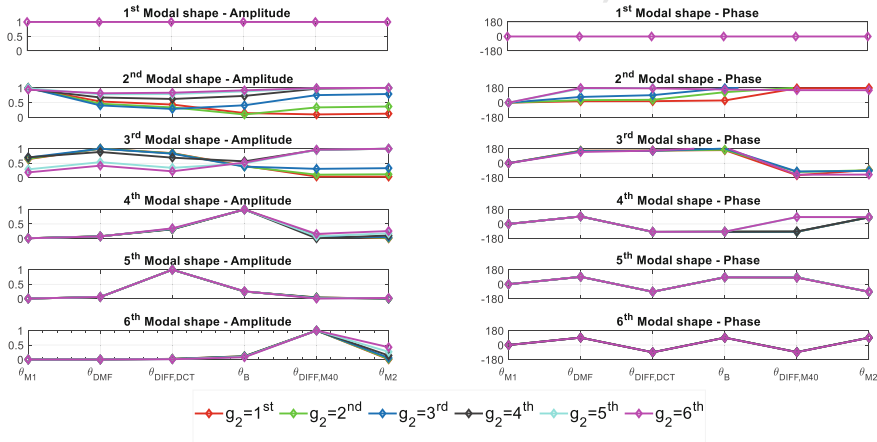


Fig. 8 Modal shape amplitude and phase of the open-loop system with different MT gears and DCT gear $g_1 = 5^{th}$

261 the modulus of the maximum element is unitary and, due to the presence of the two
 262 gear ratios τ_1 and τ_2 , they are reduced to the shaft of the electric motor M1. As an
 263 example, the r_{ih} eigenvector $\psi_{r,M1}$ is scaled as follows:

$$265 \quad \psi_{r,M1} = \left\{ \psi_1 \ \psi_2 \ \psi_3 \tau_1 \ \psi_4 \tau_1 \ \psi_5 \tau_1 \ \psi_6 \frac{\tau_1}{\tau_2} \right\}_r^T \quad (5)$$

266 The first mode represents a rigid body mode while the second mode represents
 267 the first real torsional mode of the system. The effect of the MT gear ratio mainly
 268 influences the second and third modes whereas it does not show a similar influence

269 for higher vibration modes. The last three modes show a very similar characteristic:
 270 a single inertia vibrates with respect to the remaining part of the driveline, which
 271 stays practically stationary.

272 A similar sensitivity analysis is conducted for the DCT gear g_1 , thus obtaining
 273 the results shown in Figs. 9 and 10.

274 Even in this case, the DCT gear only influences the second and the third modal
 275 shapes while higher frequency modes are not affected. Furthermore, the DCT archi-
 276 tecture with different torque paths through the transmission, depending on the gear
 277 engaged, leads to a non-monotonous trend of the natural frequency with the gear

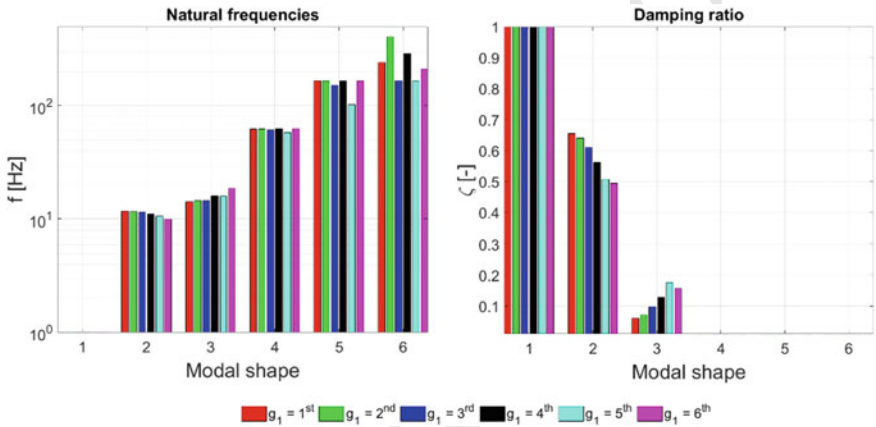


Fig. 9 Natural frequencies and damping ratio of the open-loop system with different DCT gears and MT gear $g_1 = 5th$

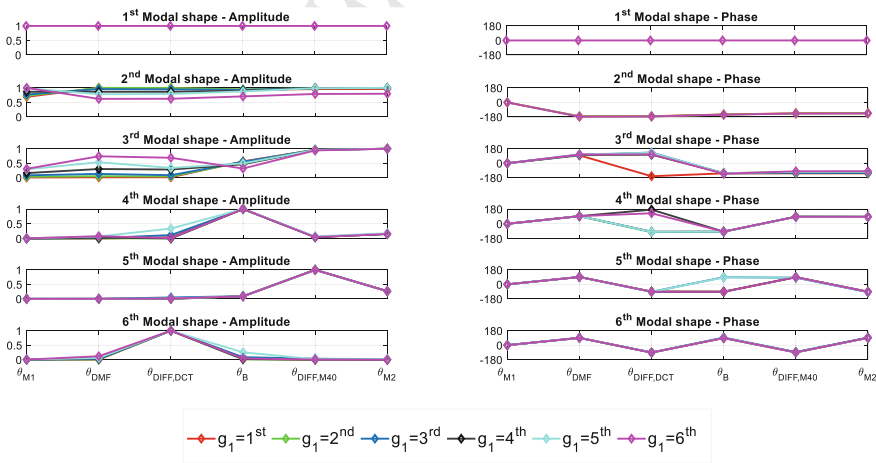


Fig. 10 Modal shape amplitude and phase of the open-loop system with different DCT gears and MT gear $g_1 = 5th$

ratio. Indeed, the even and odd gears of DCT are installed on a different input shafts if compared to the MT architecture where each gear is sequentially mounted on the unique input shaft.

3.2 Closed-Loop State-Space Model

The closed-loop system is obtained by adding the following M2 speed control logic, as shown in Fig. 6:

$$T_6 = K_p(\dot{\vartheta}_{ref} - \dot{\vartheta}_6) + K_i(\vartheta_{ref} - \vartheta_6) + K_d(\ddot{\vartheta}_{ref,F} - \ddot{\vartheta}_{6,F}) \quad (6)$$

where K_p , K_i and K_d are the proportional, the integral and the derivative gains, respectively. ϑ_{ref} is the angular position calculated from the vehicle longitudinal dynamics model, as described in Sect. 2.2. Angular accelerations $\ddot{\vartheta}_{ref,F}$ and $\ddot{\vartheta}_{6,F}$ are obtained through a band-limited derivation of $\dot{\vartheta}_{ref}$ and $\dot{\vartheta}_6$, respectively:

$$\begin{cases} t_F \ddot{\vartheta}_{ref,F} + \ddot{\vartheta}_{ref,F} = \ddot{\vartheta}_{ref} \\ t_F \ddot{\vartheta}_{6,F} + \ddot{\vartheta}_{6,F} = \ddot{\vartheta}_6 \end{cases} \quad (7)$$

where t_F is the filter time constant.

Alternative solutions exist in literature for the definition of the PID structure, e.g. the proportional and derivative terms can be placed in the feedback signal rather in the feedback error [16]. Indeed, this alternative structure provides a good disturbance rejection and removes zeros from the closed-loop transfer function thus reducing the overshoot for reference tracking response. To obtain a similar result with the standard PID structure of Eq. (6), a reference prefilter is often used. However, the PID structure selected for the presented activity is constrained by the hardware limitations imposed by the two electric motors drives with a standard control logic as in Eq. (6) with the possibility to tune the three gains and the filtering time constant.

By inserting Eqs. (6) and (7) in (1), the following 8 dynamic equations are obtained:

$$\begin{aligned} c_1 \ddot{\vartheta}_1 + c_{DMF}(\dot{\vartheta}_1 - \dot{\vartheta}_2) + c_1 \dot{\vartheta}_1 + k_{DMF}(\vartheta_1 - \vartheta_2) &= T_1 \\ I_2 \ddot{\vartheta}_2 + \left(c_2 + \frac{c_{GB1}}{\tau_1^2} \right) \ddot{\vartheta}_2 - c_{DMF}(\dot{\vartheta}_1 - \dot{\vartheta}_2) - \frac{k_{GB1}}{\tau_1} \left(\vartheta_3 - \frac{\vartheta_2}{\tau_1} \right) - k_{DMF}(\vartheta_1 - \vartheta_2) &= 0 \\ I_3 \ddot{\vartheta}_3 + c_3 \dot{\vartheta}_3 + c_{SA1}(\dot{\vartheta}_3 - \dot{\vartheta}_4) + k_{GB1} \left(\vartheta_3 - \frac{\vartheta_2}{\tau_1} \right) + k_{SA1}(\vartheta_3 - \vartheta_4) &= 0 \\ I_4 \ddot{\vartheta}_4 + c_4 \dot{\vartheta}_4 + c_{SA1}(\dot{\vartheta}_4 - \dot{\vartheta}_3) + c_{SA2}(\dot{\vartheta}_4 - \dot{\vartheta}_5) + k_{SA1}(\vartheta_4 - \vartheta_3) + k_{SA2}(\vartheta_4 - \vartheta_5) &= 0 \\ I_5 \ddot{\vartheta}_5 + c_5 \dot{\vartheta}_5 + c_{SA2}(\dot{\vartheta}_5 - \dot{\vartheta}_4) + k_{GB2} \left(\vartheta_5 - \frac{\vartheta_6}{\tau_2} \right) + k_{SA2}(\vartheta_5 - \vartheta_4) &= 0 \\ I_6 \ddot{\vartheta}_6 + \left(c_6 + \frac{c_{GB2}}{\tau_2^2} + K_p \right) \ddot{\vartheta}_6 - \frac{k_{GB2}}{\tau_2} \vartheta_5 + \left(\frac{k_{GB2}}{\tau_2^2} + K_i \right) \vartheta_6 + K_d \ddot{\vartheta}_{6,F} - K_d \ddot{\vartheta}_{ref,F} &= K_p \dot{\vartheta}_{ref} + K_i \vartheta_{ref} \end{aligned}$$

$$I_{6'} \ddot{\vartheta}_{6,F} + \left(c_6 + \frac{c_{GB2}}{\tau_2^2} + K_p \right) \dot{\vartheta}_6 - \frac{k_{GB2}}{\tau_2} \vartheta_5 + \left(\frac{k_{GB2}}{\tau_2^2} + K_i \right) \vartheta_6 + (I_6 + K_d) \ddot{\vartheta}_{6,F} - K_d \ddot{\vartheta}_{ref,F} = K_p \dot{\vartheta}_{ref} + K_i \vartheta_{ref}$$

$$I_F \ddot{\vartheta}_{ref,F} + \ddot{\vartheta}_{ref,F} = \ddot{\vartheta}_{ref}$$
(8)

The introduction of the two additional differential equations in Eq. (7) increases the state vector dimension of the closed-loop system by including the two additional states $\ddot{\vartheta}_{6,F}$ and $\ddot{\vartheta}_{ref,F}$. The tuning of proportional, integral and derivative gains modifies the equivalent damping, stiffness and inertial characteristics of the 6-DOF model. The state-space representation of the closed-loop system is then given by:

$$\dot{\mathbf{x}}_a = \mathbf{A}_{CL} \mathbf{x}_a + \mathbf{B}_{CL} \mathbf{u}_a$$
(9)

where $\mathbf{x}_a = \{ \mathbf{x}^T \ddot{\vartheta}_{6,F} \ddot{\vartheta}_{ref,F} \}^T$ is the augmented state vector and $\mathbf{u}_a = \{ T_1 \vartheta_{ref} \dot{\vartheta}_{ref} \ddot{\vartheta}_{ref} \}^T$ is the augmented input vector. Matrices \mathbf{A}_{CL} and \mathbf{B}_{CL} of the closed-loop system are defined in the Appendix.

Modal Analysis

The complex modal analysis for the closed-loop system in Eq. (9) was carried out and the results for MT gear influence are shown in Figs. 11 and 12 while the DCT gear effect is reported in Figs. 13 and 14. It is important to remark that all simulation results shown in the rest of this subsection are obtained by setting the PID gains to their optimal value reported in Table three; the tuning procedure that led to those controller parameters will be described in Sect. 4.2.

By comparing the closed-loop results in Fig. 12 with the open-loop analysis in Fig. 8, the presence of the speed controller on the motor M2 introduces an additional vibration mode which is represented by the closed-loop second modal shape

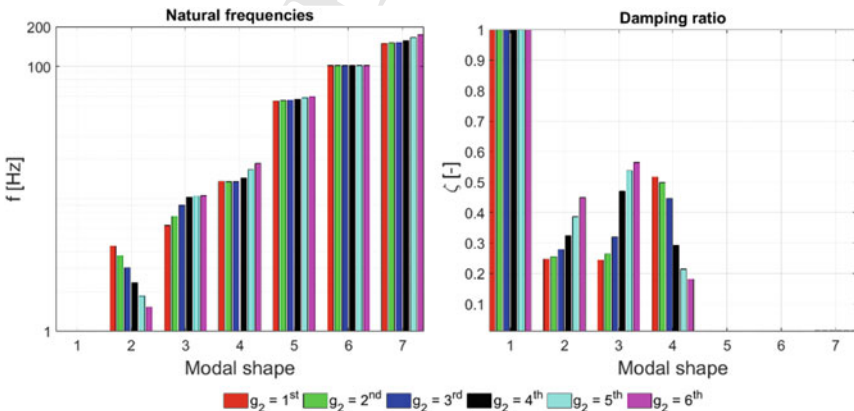


Fig. 11 Natural frequencies and damping ratio of the closed-loop system with different MT gears and DCT gear $g_1 = 5^{th}$

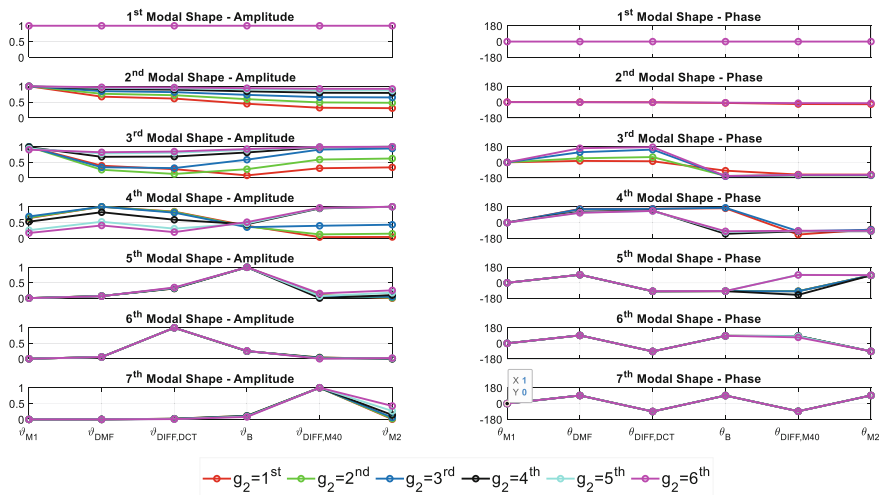


Fig. 12 Modal shape amplitude and phase of the closed-loop system with different MT gears and DCT gear $g_1 = 5th$

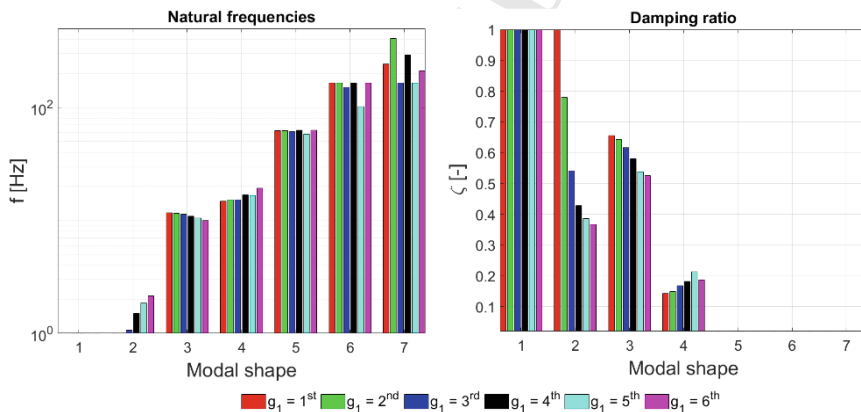


Fig. 13 Natural frequencies and damping ratio of the closed-loop system with different DCT gears and MT gear $g_2 = 5th$

333 at lower frequencies. The closed-loop modal shapes from the third to the seventh
 334 modes corresponds to the open-loop modal shapes from the second to the sixth,
 335 respectively. The speed control logic has also a small impact on the natural frequencies
 336 while the damping factor of the closed-loop third mode is increased with respect
 337 to the correspondent open-loop second mode. It is interesting to note that the speed
 338 controller does not influence the modal shape, natural frequency, and damping factor
 339 of the last three modes.

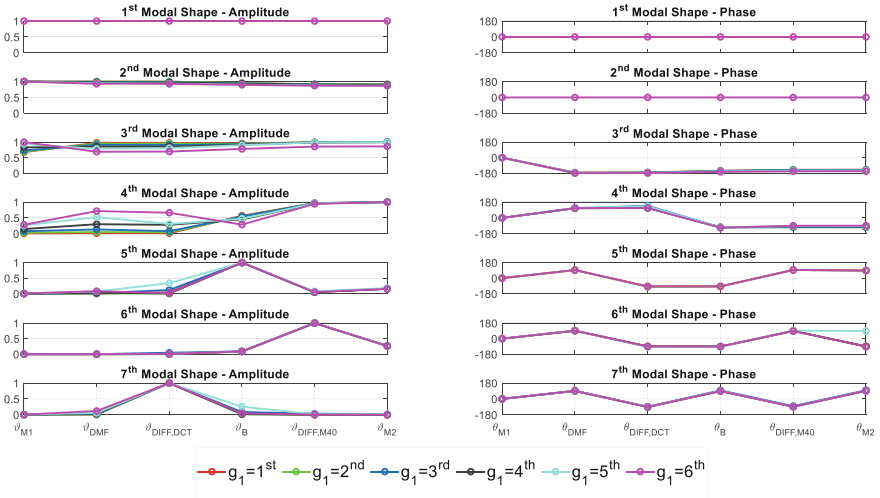


Fig. 14 Modal shape amplitude and phase of the open-loop system with different DCT gears and MT gear $g_2 = 5^{th}$

340 The effect of the DCT gear g_1 on the open-loop and the closed-loop modal analysis
 341 comparison is analyzed in Figs. 13 and 14.

342 The DCT gear ratio has a lower influence on the modal shape of the additional
 343 mode (the second) introduced by the closed-loop system. Even if the closed-loop is
 344 still beneficial in increasing the damping factor of the third and fourth modes, respect
 345 to the equivalent second and third open-loop modes, the variation of the DCT gear
 346 ratio is not as effective as observed for the variation of the MT gear.

347 3.3 Model Experimental Validation

348 A torsional vibration test is executed on the DCT test rig to obtain the experimental
 349 data and validate the linear model described and analyzed in the previous sections.
 350 During the test, one electric motor (e.g. M2) is controlled to apply a sinusoidal torque
 351 with a constant amplitude and a continuously variable frequency, while the second
 352 motor (M1) is controlled to keep a constant speed. Before the torsional vibration
 353 test is started, a preliminary phase is required to bring the transmission test rig into a
 354 steady-state condition, identified by constant torque and speed, where the behavior of
 355 the system can be linearized through Eq. (1). The preliminary phase is fundamental
 356 to keep approximately constant the system parameters, e.g. torsional stiffnesses, and
 357 to avoid any inversion of torque sign thus preventing nonlinear phenomena such as
 358 the impact between rotating components due to backlash.

Time histories of the torques applied by the two electric motors are measured together with the angular speeds in three points of the transmission line ($\dot{\theta}_1 = \dot{\theta}_{M1}$, $\dot{\theta}_3$, and $\dot{\theta}_6 = \dot{\theta}_{M2}$).

The sinusoidal torque applied by the M2 motor is:

$$T_6 = \bar{T} + T_0 \sin(2\pi f(t)t) \quad (10)$$

where \bar{T} is a mean value of torque constantly applied during the test to create a torsional preload in the transmission system (to avoid nonlinearities), T_0 is the torque amplitude and $f(t)$ the excitation frequency calculated as a power function of the time t (logarithmic chirp):

$$f(t) = f_0 \left(\frac{f_1}{f_0} \right)^{\frac{t}{t_1}} \quad (11)$$

where f_0 is the initial frequency and f_1 is the final frequency at time t_1 .

Experimental measurements are then processed resulting in the Frequency–Response Functions (FRFs) between the input torque T_6 applied by M2 and the three rotational speeds. Under the assumption that the system is linear (at least in the neighborhood of the equilibrium point around which the system vibrates) and characterized by time-invariant parameters, the estimation of a FRF from experimental data can be performed by calculating the Power Spectral Density (PSD) and the Cross-Power Spectral Density (CSD) through the Welch’s method [17].

Figures 15 and 16 show the estimated FRFs from the measurements together with their coherence functions to evaluate the frequency range for which the estimation algorithm is considered reliable.

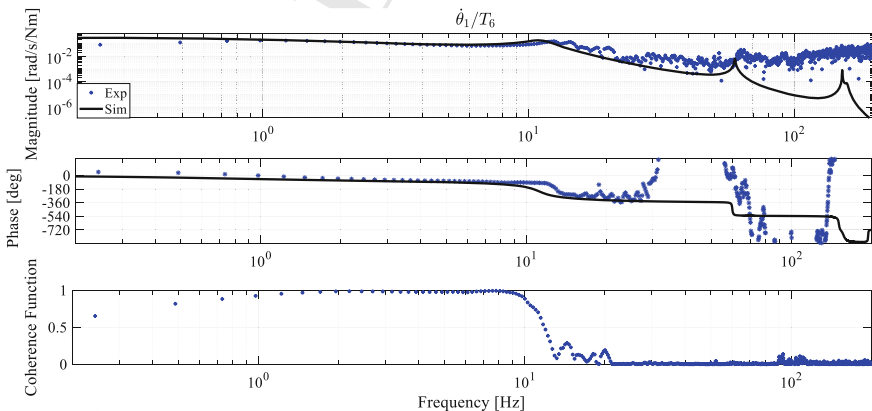


Fig. 15 FRF $\dot{\theta}_1/T_6$ resulting from the experimental measurements and calculated using the open-loop linear model with $g_1 = 3rd$ and $g_2 = 4th$

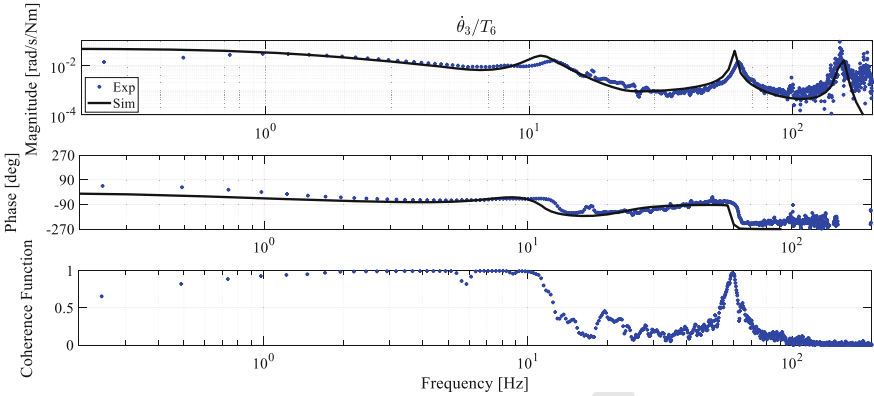


Fig. 16 FRF $\dot{\theta}_3/T_6$ estimated from the experimental measurements and calculated from the open-loop linear model with $g_1 = 3rd$ and $g_2 = 4th$

382 Since the excitation for the dynamic system is generated by the electric motor
 383 M2, the amplitude of the $\dot{\theta}_3/T_6$ and $\dot{\theta}_6/T_6$ responses are high enough to be measured
 384 accurately by the encoder up to more than 150 Hz. On the other hand, the lower
 385 amplitude of oscillation for the other M1 motor limits the range of reliability of
 386 $\dot{\theta}_1/T_6$ to 20 Hz.

387 The results concerning the first FRF ($\dot{\theta}_1/T_6$) are affected by a relevant phase
 388 difference in the high frequency range, and this is mainly due to very low signal to
 389 noise ratio in the experimental measures rather than to the model, as also confirmed
 390 by the coherence function that drops to zero very quickly after 20 Hz.

391 On the other hand, the experimental FRF of $\dot{\theta}_3/T_6$ is very well estimated from the
 392 encoder measurements in the whole frequency range, thanks to the high peak ampli-
 393 tudes and the high encoder resolution. Furthermore, the linear model can capture
 394 both the experimental magnitude and phase up to more than 200 Hz.

395 Finally, the FRF of $\dot{\theta}_6/T_6$ is shown in Fig. 17, where the accuracy of the experi-
 396 mental estimation decreases significantly immediately after the third peak in magni-
 397 tude. However, the FRF magnitude and phase is also well captured by the linear
 398 model within the validation range of the experimental estimation.

399 4 Sensitivity Analysis of the Linear Model

400 The experimentally validated DCT torsional model represents an important tool for
 401 predicting and calibrating the effect of the two motor controllers on the test rig
 402 dynamic behavior. The present section aims at analyzing the DCT model sensitivity
 403 to the parameters that are subject to calibration, e.g. the speed control logic gains, or
 404 to optimization for accomplishing the desired operative condition, e.g. the DCT or
 405 MT gear ratio.

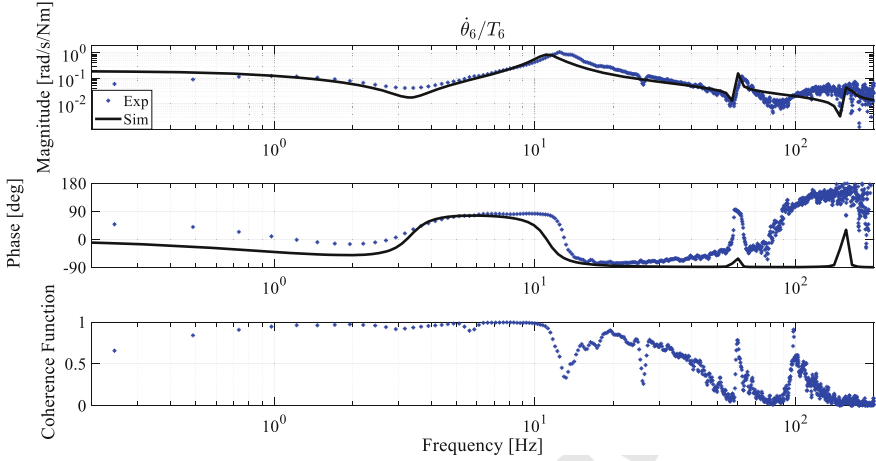


Fig. 17 FRF $\dot{\theta}_6/T_6$ estimated from the experimental measurements and calculated from the open-loop linear model with $g_1 = 3rd$ and $g_2 = 4th$

406 The sensitivity analysis is carried out in the frequency domain by considering
 407 the frequency response functions between the closed-loop system input (M1 motor
 408 torque T_1 and reference speed $\dot{\theta}_{ref}$) and the desired output quantities selected for
 409 evaluating the DCT test rig performance. One of the main tasks for the considered
 410 HiL test rig is to regulate the brake disk speed $\dot{\theta}_4$ to track the reference angular speed
 411 calculated from the vehicle model. However, the speed control logic in Eq. (6) is
 412 applied to the M2 motor speed $\dot{\theta}_6$. Based on these considerations, four FRFs are
 413 evaluated from the closed-loop system described by the state space in Eq. (9): two
 414 Reference Speed Tracking (RST) FRFs for evaluating the controller tracking perform-
 415 ance and two Disturbance Rejection (DR) FRFs for analyzing the M2 controller
 416 sensitivity to the application of the M1 motor torque.

417 The two RST FRFs are obtained by considering a harmonic excitation for the
 418 reference speed $\dot{\theta}_{ref}$ with amplitude $\dot{\theta}_{ref,0}$ and frequency Ω by fixing the M1 torque
 419 $T_1 = 0$:

$$420 \quad \alpha_{RST}(\Omega) = [G_{RST}^4(\Omega) \ G_{RST}^6(\Omega)]^T = C(j\Omega I - A_{CL})^{-1} B_{CL} [0 \ 1/(j\Omega) \ 1 \ j\Omega]^T \quad (12)$$

422 where $C = [0 \ 0 \ 0 \ 0 \ 0 \ 0 \ 0 \ 0 \ 0 \ 1 \ 0 \ 1 \ 0 \ 0]^T$ is the output matrix; $G_{RST}^4 =$
 423 $\tau_2 \dot{\theta}_{4,0}/\dot{\theta}_{ref,0}$ and $G_{RST}^6 = \dot{\theta}_{6,0}/\dot{\theta}_{ref,0}$ are the RST FRFs from the reference speed
 424 to the disk brake $\dot{\theta}_4$ and to the M2 motor speed $\dot{\theta}_6$, respectively.

425 The desired shape for both the RST FRFs is $G_{RST}^4(\Omega) = G_{RST}^6(\Omega) = 1$ for
 426 $\Omega < \Omega_B$ where Ω_B represents the closed-loop bandwidth frequency above which it
 427 is required to drop for reducing the sensitivity to high frequency noises.

428 The two DR FRFs are computed by considering a harmonic excitation for the
 429 M1 torque T_1 with amplitude $T_{1,0}$ and frequency Ω by fixing the reference speed
 430 $\theta_{ref} = \dot{\theta}_{ref} = \ddot{\theta}_{ref} = 0$:

432
$$\alpha_{DR}(\Omega) = [G_{DR}^4(\Omega) G_{DR}^6(\Omega)]^T = C(j\Omega I - A_{CL})^{-1} B_{CL} [1 \ 0 \ 0 \ 0]^T \quad (13)$$

433 where $G_{DR}^4 = \dot{\theta}_{4,0}/T_{1,0}$ and $G_{DR}^6 = \dot{\theta}_{6,0}/T_{1,0}$ are the DR FRFs from the M1 torque
 434 T_1 to the disk brake $\dot{\theta}_4$ and to the M2 motor speed $\dot{\theta}_6$, respectively.

435 The desired shape for both the DR FRFs is $G_{DR}^4(\Omega) = G_{DR}^6(\Omega) = 0$ for the
 436 whole frequency range.

437 **4.1 Sensitivity to Gear Ratios**

438 The first analysis concerns the model sensitivity to the variation of the DCT gear
 439 ratio, which is a parameter imposed by the TCU having a strong influence on the test
 440 bench dynamics and the motor controller performance. The PID gains of the speed
 441 controller are set to the nominal values reported in Table three.

442 Figure 18 shows the trend of the RST and DR FRFs when the DCT gear ratio is
 443 changed, and the MT gear ratio is kept constant to $g_2 = 5th$.

444 Both RST FRFs show a clear resonance peak at the first natural frequency that
 445 increases with the DCT gear ratio, as already shown in Fig. 13. The amplitude of
 446 the first resonance peak increases with the DCT gear ratio thus reflecting the

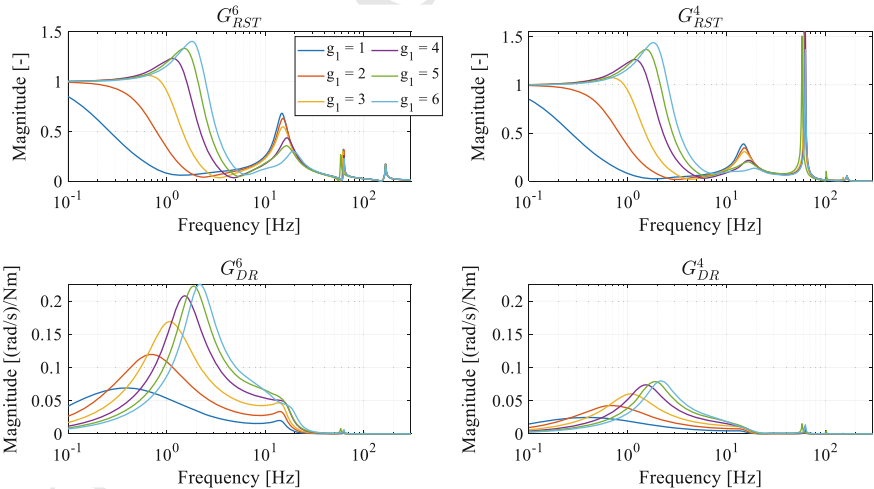


Fig. 18 DR and RST FRFs magnitude for the closed-loop system with different DCT gears and MT gear $g_2 = 5th$

damping ratio characteristics obtained from the modal analysis in Fig. 13. A second resonance peak is also visible for the G_{RST}^6 FRF whose frequency increases with the DCT gear but its amplitude decreases for higher gears. A similar shift of the resonance frequencies is obtained for the G_{RST}^4 FRF but the amplitude of the second and the third peaks are more pronounced than their correspondents in G_{RST}^6 . This result agrees with the modal shape of the fifth mode (~ 60 Hz) in Fig. 14 where the brake disk inertia vibrates with respect to the remaining part of the driveline, which stays practically stationary.

The effect of the motor M1 torque is analyzed through the two DR FRFs plotted in Fig. 18. The influence of the M1 torque on $\dot{\theta}_6$ and $\dot{\theta}_4$ dynamics is more pronounced for G_{DR}^6 than G_{DR}^4 and amplifies the first peak for higher DCT gears.

The main conclusion for the sensitivity analysis on the DCT gear variation is that the dynamic behavior of the M2 speed controller is improved in terms of disturbance rejection from M1 when the first gear is engaged in the DCT. However, the reference tracking attitude for $g_1 = 1$ does not represent the best selection since the closed-loop bandwidth is drastically reduced if compared to higher gears RST FRFs.

The second sensitivity analysis involves the variation of the MT gear ratio, considered as a tunable parameter for extending the test rig operative speed and torque range based on the maneuver selection. The effect of τ_2 on the RST FRFs is shown in Fig. 19 by engaging the fifth DCT gear.

The effect of MT gear on the first peak of both G_{RST}^6 and G_{RST}^4 is opposite if compared to the DCT sensitivity analysis in Fig. 18: the resonance frequency and the peak amplitude decreases with MT gear. Moreover, the first and second peaks tends to get closer for lower gears so that they produce a single peak for G_{RST}^6 when $g_2 = 1$. The sixth gear would represent a good choice in terms of reference tracking

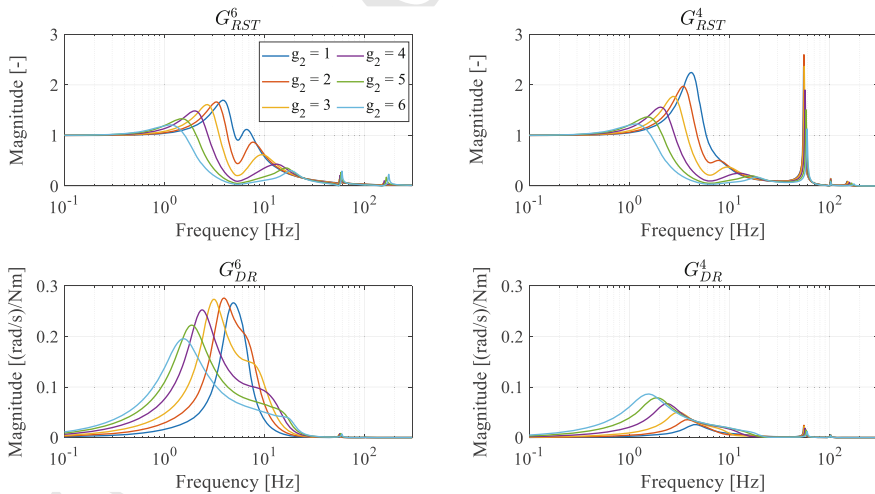


Fig. 19 RST and DR FRFs magnitude for the closed-loop system with different MT gears and DCT gear $g_1 = 5th$

472 performance due to the lower amplitude of the first peak, even if this advantage is
 473 obtained with a lower closed-loop bandwidth, if compared to other gears. Finally,
 474 the DR FRFs modification to the MT gear ratio variation is reported in Fig. 19. The
 475 influence of M1 torque on the M2 speed controller dynamics is still more predominant
 476 on G_{DR}^6 than G_{DR}^4 . The selection of higher gears reduces the first peak amplitude for
 477 G_{DR}^6 while a lower gear is beneficial for attenuating G_{DR}^4 .

478 The sensitivity analysis on the MT gear ratio variation led to the conclusion that
 479 the sixth gear represents an optimal solution to always guarantee the desired reference
 480 tracking performance and external disturbance rejection. However, the actual usage
 481 of the HiL test bench requires to run the desired maneuver considering also the
 482 constraints imposed by the power and torque limitations of the two electric motors,
 483 that may require a different gear selection from the optimal solution. Therefore,
 484 the performance of the test bench must be carefully verified with all the possible
 485 combinations of gear ratios.

4.2 Sensitivity to PID Gains

487 Differently from the mechanical parameters such as the DCT and MT gear ratios, the
 488 PID gains as well as the filter time constant t_F , can be tuned and eventually adapted
 489 to the test rig operative conditions with more flexibility.

490 The effect of the speed proportional gain K_p on the RST FRFs is evaluated in
 491 Fig. 20 where the fifth gear is set for both DCT and MT.

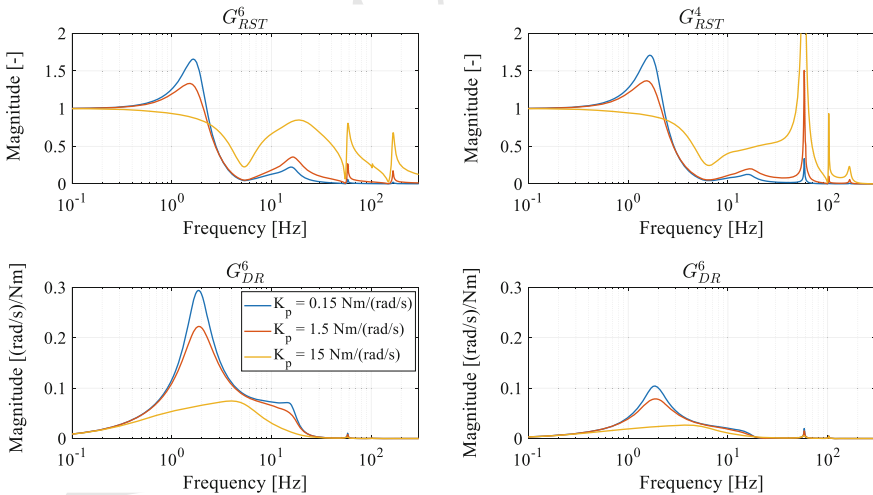


Fig. 20 RST and DR FRFs magnitude for the closed-loop system with different proportional gains K_p , by setting $K_i = 75 \text{ Nm/rad}$, $K_d = 0.75 \text{ Nm/(rad/s}^2)$, $t_F = 100 \text{ s}$, $g_1 = 5th$ and $g_2 = 5th$

492 The proportional speed gain cannot shift none of the resonance frequencies refer-
 493 ring to both G_{RST}^6 and G_{RST}^4 but it can modify their amplitude values. The reason
 494 behind that is well explained by Eq. (8) where K_p modifies the multiplicative coeffi-
 495 cient of $\dot{\theta}_6$. An increment of K_p would improve the reference tracking performance
 496 by reducing the first peak amplitude and by extending the closed-loop bandwidth.
 497 However, the benefits achieved with a high K_p gain on the G_{RST}^6 FRF produces a
 498 negative effect on the G_{RST}^4 FRF for the high frequency range. This aspect aims at
 499 remarking that even a fine tuning of the M2 speed controller may provoke excessive
 500 oscillations in other driveline parts and then transmitted to the test rig supports in
 501 terms of vibrations or noises perceived by the user. A similar sensitivity analysis
 502 for the disturbance rejection FRFs is shown in Fig. 20 where an increment of K_p is
 503 positive for both G_{DR}^6 and G_{DR}^4 in terms of resonance peak attenuation.

504 The effect of the integral gain K_i on the RST and DR FRFs is then evaluated in
 505 Fig. 21.

506 Differently from the proportional gain, the integral contribution can shift the
 507 resonance frequency of the first peak since it modifies the stiffness contribution in
 508 Eq. (8) for the last degree of freedom (motor M2). The main benefit of increasing the
 509 integral gain is the extension of the closed-loop bandwidth but at the cost of a more
 510 pronounced peaks amplitude in the whole frequency range. An increment of K_i also
 511 produces a shift of the DR FRFs first resonance peak towards higher frequencies and
 512 it shrunk the frequency band around the peak, as visible for both G_{DR}^6 and G_{DR}^4 .
 513 Another benefit from the increment of the integral contribution is the attenuation of
 514 the G_{DR}^6 peak amplitude meanwhile G_{DR}^4 amplitude is not influenced by the variation
 515 of this parameter.

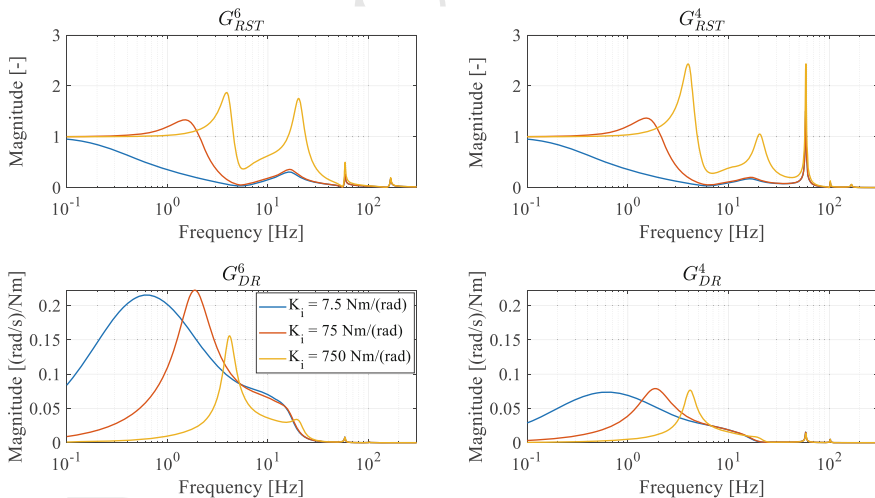


Fig. 21 RST FRFs magnitude for the closed-loop system with different integral gains K_i , by setting $K_p = 1.5 \text{ Nm}/(\text{rad/s})$, $K_d = 0.75 \text{ Nm}/(\text{rad/s}^2)$, $t_F = 100 \text{ s}$, $g_1 = 5th$ and $g_2 = 5th$

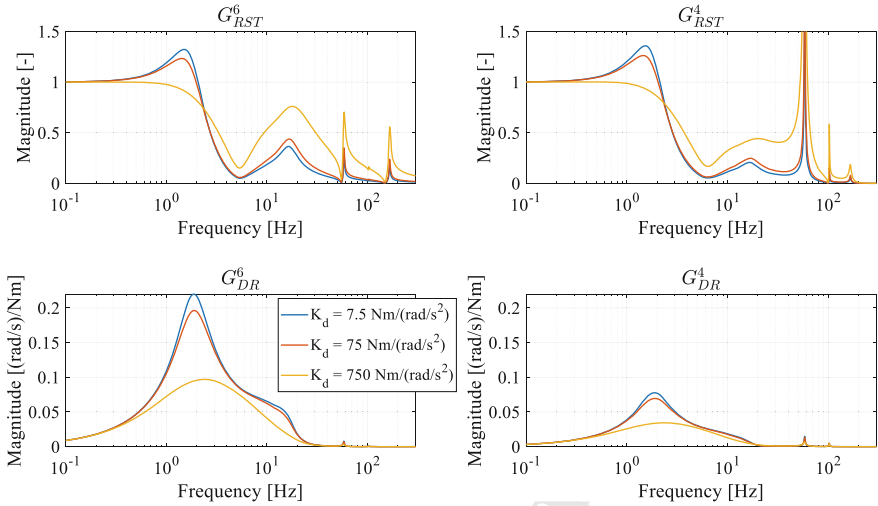


Fig. 22 RST and DR FRFs magnitude for the closed-loop system with different derivative gains K_d , by setting $K_p = 1.5 \text{ Nm/(rad/s)}$, $K_i = 75 \text{ Nm/rad}$, $t_F = 100 \text{ s}$, $g_1 = 5th$ and $g_2 = 5th$

516 Furthermore, the effect of the derivative PID gain on both RST and DR FRFs is
 517 shown in Fig. 22.

518 The derivative gain can modify the peaks amplitude, but it cannot shift any resonance
 519 frequency. The positive benefit of a high derivative gain is the reduction of the
 520 first peak magnitude for both G_{RST}^6 and G_{RST}^4 but at the cost of an increment in the
 521 peak amplitudes for higher frequencies, especially for G_{RST}^4 . A similar conclusion
 522 is observed for the DR FRFs, where an increment of K_d is beneficial for the whole
 523 frequency range in terms of peak attenuation but at the cost of a larger frequency
 524 band pass.

525 Finally, the impact of the filter time constant t_F on both RST and DR FRFs is
 526 illustrated in Fig. 23. It can be seen that, the effect of the filter time constant on system
 527 dynamics in the low-mid frequency range is non monotonic: for low values of t_F , an
 528 additional damping to the first resonant mode is obtained; on the contrary, for high
 529 values, a further increase reduces the damping and increases the frequency of the
 530 main peaks of all the considered FRFs. On the other hand, at high frequencies, the
 531 effect of the time constant increment is always to attenuate the response of both RST.
 532 This last effect is particularly beneficial in this application, where high frequency
 533 disturbances are generated by the staircase encoder speed signals that requires to
 534 filter out this high frequency content to avoid NVH issues during the test.

535 The results obtained through the sensitivity analysis of the M2 speed controller
 536 parameters, represent a valid tool for calibrating the PID gains thus achieving a
 537 closed-loop FRF response which can be shaped according to the desired requirements
 538 reported in Table 2. The desired shape for both G_{RST}^6 and G_{RST}^4 FRFs magnitudes
 539 should be constrained as close as possible to 1 to satisfy the reference tracking
 540 performance. However, this can be achieved only within the frequency bandwidth

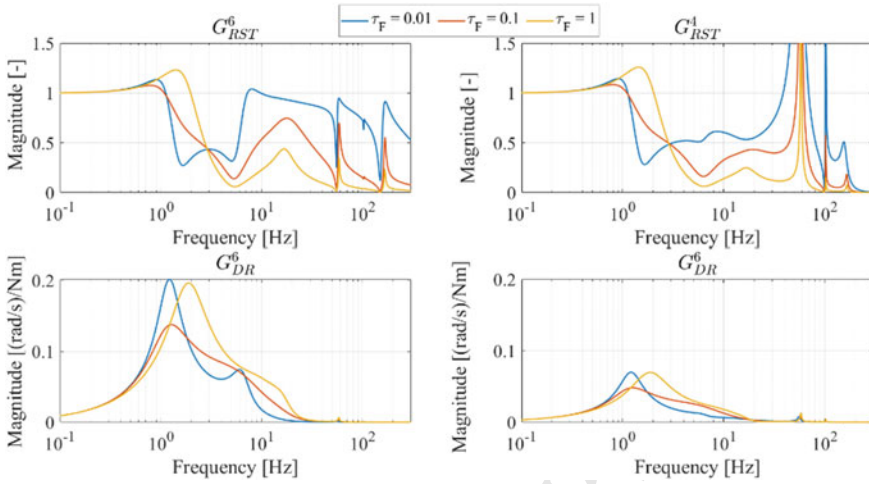


Fig. 23 RST and DR FRFs magnitude for the closed-loop system with different filter time constant t_F , by setting $K_p = 1.5$ Nm/(rad/s), $K_i = 75$ Nm/rad, $K_d = 0.75$ Nm/(rad/s²), $g_1 = 5th$ and $g_2 = 5th$

Table 2 Desired FRF requirements for PID calibration

Property	Requirements
Peak amplitude of G^6_{RST}	≤ 1.3
Peak amplitude of G^4_{RST}	≤ 1.5
Bandwidth of G^6_{RST} (at half-power point)	≥ 2 Hz
Bandwidth of G^6_{DR} (at half-power points)	≤ 4 Hz
Peak amplitude of G^6_{DR}	≤ 0.25 (rad/s)/Nm

range, that is the frequency range where the magnitude of a closed-loop FRF is greater than -3 dB. The sensitivity analysis shows that the most effective parameter to extend the frequency bandwidth is the integral contribution K_i . An excessive selection of the integral gain produces an increment of all resonance peak amplitudes, thus reducing the reference tracking performance. This negative consequence can be in part compensated by increasing the proportional and the derivative gains to smooth the peaks, at least in the lower frequency range. The amplitude of the G^4_{RST} peaks also require a constraint to avoid an undesired vibration level in any other point of the driveline. Indeed, since the closed-loop system is feedbacked on the M2 motor speed, the magnitude constraint for G^4_{RST} peaks is set higher than G^6_{RST} FRF.

To keep the desired reference tracking performance achieved for RST FRFs, the influence of the M1 motor torque should be also mitigated by shaping G^6_{DR} and G^4_{DR} . The sensitivity analysis proved that G^6_{DR} represents the more critical FRF in terms of resonance peaks amplitude and on the peak frequency band which can be shrunk

Table 3 Final values of PID gains

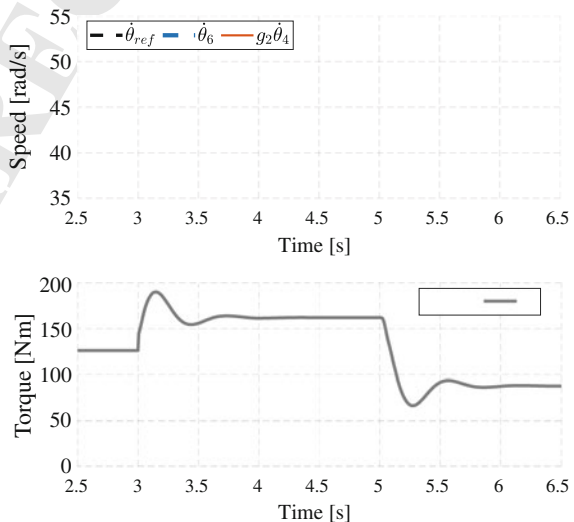
Gain	Value
Proportional gain K_p	1.5 Nm/(rad/s)
Integral gain K_i	75 Nm/(rad)
Derivative gain K_d	0.75 Nm/(rad/s ²)
Derivative time constant t_F	100 s

555 with an increment of the integral gain and a reduction of proportional and derivatives
 556 gains.

557 To achieve the required dynamic performance of the closed-loop system reported
 558 in Table 3, a brute force method is applied to search for a suitable set of PID gains
 559 among a predefined range of values. The lower and the upper limits of each PID
 560 parameter range are defined based on the sensitivity analysis carried out in the present
 561 section, thus constraining the brute force algorithm to test only the set of gains that
 562 provoke a perceptible variation of the RST and DR frequency responses. The final
 563 gains computed by the brute force algorithm are then reported in Table 3:

564 The final set of PID parameters clearly shows that the solution computed by
 565 the brute force algorithm provides a low derivative gain with a high filtering time
 566 constant, whose combined effect produces a negligible intervention of the derivative
 567 term. Indeed, Fig. 22 clearly demonstrates that only a derivative gain of two magni-
 568 tude order greater than the nominal value would modify the frequency response of
 569 the closed-loop system. The calibrated speed controller is then verified through the
 570 time domain response of the closed-loop system, by providing a delayed step input
 571 between $\dot{\theta}_{ref}$ and T_1 . Time histories results of $\dot{\theta}_6$, $\dot{\theta}_4$ and T_6 are shown in Fig. 24.

Fig. 24 Time response of $\dot{\theta}_6$ and $\dot{\theta}_4$ to a delayed step input between $\dot{\theta}_{ref}$ and T_1 with $g_1 = 5th$ and $g_2 = 5th$



572 The speed controller on M2 provides satisfactory response in terms of reference
 573 speed tracking performance with an overshoot of 5.6%, a rise time of 0.2 s and a
 574 settling time of 0.4 s. The step torque on T_1 , applied 2 s later after the imposition of
 575 the step on the reference speed, provides useful information regarding the capability
 576 of the controller to react to external disturbance. Even if the M1 torque T_1 produces a
 577 16% overshoot on $\dot{\theta}_6$ and $\dot{\theta}_4$, the closed-loop system can reject the torque disturbance
 578 after 1 s.

579 5 Controller Experimental Validation

580 The PID gains selected through the sensitivity analysis described in the previous
 581 section, are then implemented to the transmission test rig for validating the controller
 582 performance. The controller performance is validated both in frequency and time
 583 domain to prove its efficiency in terms reference tracking accuracy and disturbance
 584 rejection to external torques. To guarantee that the transmission works as much as
 585 possible in a linear operating range, before the execution of any experiments, the test
 586 rig is brought into a steady-state condition identified by a constant angular speed,
 587 imposed by the speed controller of M2, and by a transmission torsional preload
 588 through the application of a constant torque from the motor M1. This procedure is
 589 necessary to avoid the inversion of the torque sign which is responsible for extremely
 590 non-linear gear teeth impact due to the torsional backlashes between transmission
 591 rotating components [11, 18].

592 During the first test, the M2 electric motor is controlled in speed through the PID
 593 logic in Eq. (6) and parametrized according to Table 3. A sinusoidal speed with a
 594 constant amplitude and a continuously variable frequency is generated for $\dot{\theta}_{6,ref}$:

$$596 \quad \dot{\theta}_{ref} = \dot{\theta}_m + \dot{\theta}_a \sin(2\pi f(t)t) \quad (14)$$

597 where $\dot{\theta}_m$ and $\dot{\theta}_a$ are the mean and the amplitude values of the sinusoidal signal,
 598 respectively. $f(t)$ is calculated to obtain a logarithmic chirp as described in Eq. (11).
 599 The second motor (M1) is controlled to apply a constant torque T_1 to guarantee the
 600 desired preload. The measured M2 motor speed is then elaborated, together with
 601 $\dot{\theta}_{ref}$, to estimate the experimental RST FRF, according to the algorithm described in
 602 Sect. 3.3. The experimental estimation of G_{RST}^6 is then compared to the linear model
 603 RST FRF in Fig. 25.

604 The experimental G_{RST}^6 is well estimated up to 40 Hz, above which the coher-
 605 ence function drops to zero. The good match between the experimental FRF with
 606 the linear model response proves that the PID gains tuned through the sensitivity
 607 analysis described in Sect. 4, can guarantee the desired RST performance also for
 608 the transmission test rig.

609 The M2 speed controller is furtherly investigated through a second experiment that
 610 aims at validating its robustness against the application of a dynamic external torque

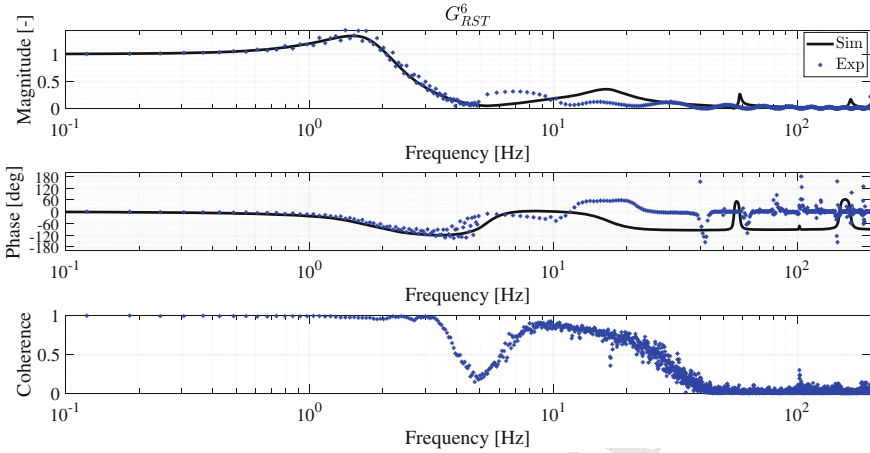


Fig. 25 Experimental estimation and model evaluation of G^6_{RST} by fixing $K_p = 1.5 \text{ Nm}/(\text{rad/s})$, $K_i = 75 \text{ Nm}/\text{rad}$, $K_d = 0.75 \text{ Nm}/(\text{rad/s}^2)$, $t_F = 100 \text{ s}$ $g_1 = 5th$ and $g_2 = 5th$

611 from the electric motor M1. The M2 motor is controlled to keep a constant speed
 612 meanwhile a sinusoidal torque signal with a constant amplitude and a continuously
 613 variable frequency is applied by M1:

$$615 \quad T_1 = T_{1,m} + T_{1,a} \sin(2\pi f(t)t) \quad (15)$$

616 where $T_{1,m}$ and $T_{1,a}$ are the mean and the amplitude values of the sinusoidal signal,
 617 respectively. $f(t)$ is calculated to obtain a logarithmic chirp as described in Eq. (11).
 618 The M1 torque is measured, as well as the M2 speed $\dot{\theta}_6$, to elaborate the estimation
 619 of G^6_{DR} which is compared against the linear model DR FRF in Fig. 26.

620 Within the frequency validation range of the experimental G^6_{DR} (up to 40 Hz),
 621 the M2 speed controller shows disturbance rejection properties even better than the
 622 desired requirements imposed in Table 2 as proved by the lower peak amplitude
 623 around 2 Hz.

624 Finally, the speed controller is verified in the time domain by imposing a step
 625 signal to the reference signal $\dot{\theta}_{ref}$. The experimental time histories of the M2 motor
 626 speed is compared against the linear transmission model step response in Fig. 27.

627 The experimental M2 motor speed is characterized by a quick response during
 628 the initial phase of the step application, mainly due to the presence of the second
 629 resonance peak at $\sim 20 \text{ Hz}$ visible in Fig. 25, followed by a slower dynamics dictated
 630 by the first resonance peak at $\sim 2 \text{ Hz}$. The mismatch observed between the exper-
 631 imental and simulation results in Fig. 27 is larger than what expected from the
 632 frequency-domain comparison. This discrepancy is mainly due to the intervention
 633 of the nonlinear transmission behavior during the test execution. The main nonlin-
 634 earities in an automotive transmission system are backlashes and angular clearances
 635 between the rotating components (meshing gears and synchronizers). Indeed, the

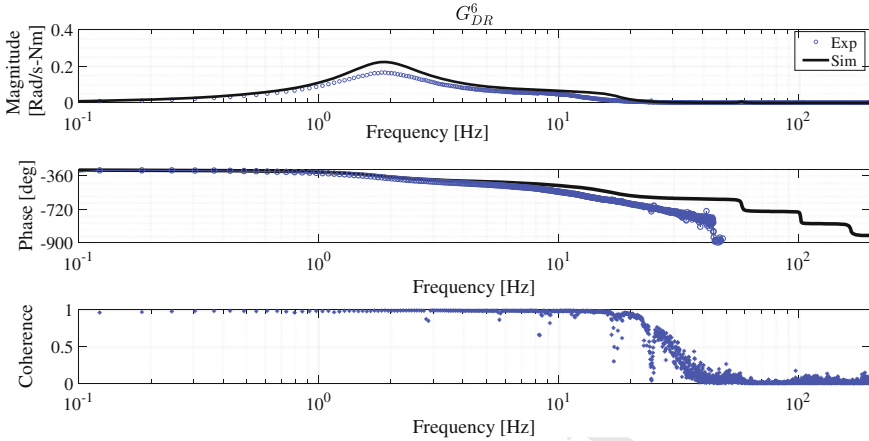


Fig. 26 Experimental estimation and model evaluation of G_{DR}^6 by fixing $K_p = 1.5 \text{ Nm}/(\text{rad/s})$, $K_i = 75 \text{ Nm}/\text{rad}$, $K_d = 0.75 \text{ Nm}/(\text{rad/s}^2)$, $t_F = 100 \text{ s}$, $g_1 = 5th$ and $g_2 = 5th$

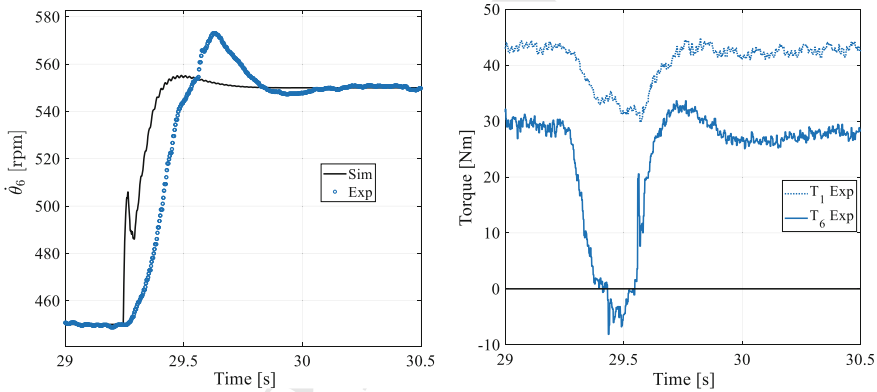


Fig. 27 Experimental and analytical time response of θ_6 , T_1 and T_6 by fixing $K_p = 7.5 \text{ Nm}/(\text{rad/s})$, $K_i = 75 \text{ Nm}/\text{rad}$, $K_d = 0.75 \text{ Nm}/(\text{rad/s}^2)$, $t_F = 100 \text{ s}$, $g_1 = 5th$ and $g_2 = 5th$

636 second subplot of Fig. 27 shows a typical nonlinear trend of the torque entering the
 637 MT gearbox. A torque sign inversion characterized by a dead band is clearly visible;
 638 it is related to a loss of contact between internal rotating components of MT gearbox
 639 due to load reversal. The loss of contact after zero crossing is followed by torsional
 640 impacts which generate peaks in the instantaneous torque trend (see also [11, 19] for
 641 further details). The effect of backlash nonlinearities is to make the MT working in
 642 an operating condition far from the linear hypothesis assumed for system modelling.
 643 Nevertheless, the performance of the controlled system in time domain is still satisfac-
 644 tory even if the system dynamic behavior is quite different from the one used for

645 controller parameter tuning. On the other hand, the sine-sweep test used for elaborating the experimental FRFs in Fig. 26, is executed with a constantly applied mean torque $T_{1,m}$ (see Eq. 10) that guarantees a minimum level of torsional preload that avoid any backlashes recovery. A similar conclusion is also valid for the sine-sweep results of Fig. 25, where the combination of a low sine amplitude $\dot{\theta}_a$ with a constant preload T_1 constrains the transmission test rig to work in a linear operating condition thus justifying a better match with the simulated FRF.

622 6 Conclusions

653 This paper provided a model-based tuning procedure for controlling the electric motors of a transmission HiL test rig with the aim of achieving the desired closed-loop requirements with the following main conclusions.

- 656 • HiL transmission test rigs require an accurate calibration of the torque and speed feedback controllers of the actuators, e.g. electric motors, used to emulate the external load applied to the system under investigation, e.g. a DCT.
- 659 • The dynamic behavior of the driveline mounted on the test bench is well described by the proposed linear 6-DOF transmission model, for both open-loop and closed-loop configurations, as long as the transmission test rig operates in linear conditions, e.g. avoiding torque sign inversion.
- 663 • The step change of the gear ratio of the transmission under test during normal operation of the bench has a relevant effect on system torsional dynamics. Potential future developments could involve an adaptation of the control parameters to achieve satisfactory performance in all the operating conditions. However, most of industrial drives typically do not allow a gain scheduling of the motor controllers during the test execution.
- 669 • A novel methodology for analyzing and tuning the reference speed tracking and disturbance rejection performance of the motor controllers, both in frequency and time domains has been explained. The sensitivity analysis helps to understand the effect of each mechanical and control parameter on the system dynamics thus guiding the calibration process.
- 674 • The application of this method to the DCT HiL test rig installed at Politecnico di Torino provided a good tradeoff between the conflicting requirements (reference speed tracking and disturbance rejection). The torsional vibration analysis of the system revealed the presence of an underdamped mode that could be excited by high frequencies noises related to speed or torque feedback signals. This requires a speed controller design that must include the analysis of the internal dynamics of the whole transmission and driveline to avoid NVH issues during normal operation of the bench.

Appendix—Closed-Loop State Space Matrices

$$A_{CL} = \begin{bmatrix} A_{11} & A_{12} & A_{13} \\ A_{21} & A_{22} & A_{23} \end{bmatrix}$$

where:

$$A_{11} = \mathbf{O}_{6 \times 6}; \quad A_{12} = \mathbf{I}_{6 \times 6}; \quad A_{13} = \mathbf{O}_{6 \times 2}$$

$$A_{21} = \begin{bmatrix} -\frac{k_{DMF}}{I_1} & \frac{k_{DMF}}{I_1} & 0 & 0 & 0 & 0 & 0 \\ \frac{k_{DMF}}{I_2} & -\left(k_{DMF} + \frac{k_{GB1}}{\tau_1^2}\right) & \frac{k_{GB1}}{\tau_1 I_2} & 0 & 0 & 0 & 0 \\ 0 & \frac{k_{GB1}}{\tau_1 I_3} & -\frac{(k_{GB1} + k_{SA1})}{I_3} & \frac{k_{SA1}}{I_3} & 0 & 0 & 0 \\ 0 & 0 & \frac{k_{SA1}}{I_4} & -\frac{(k_{SA1} + k_{SA2})}{I_4} & \frac{k_{SA2}}{I_4} & 0 & 0 \\ 0 & 0 & 0 & \frac{k_{SA2}}{I_5} & -\frac{(k_{SA2} + k_{GB2})}{I_5} & \frac{k_{GB2}}{\tau_2 I_5} & 0 \\ 0 & 0 & 0 & 0 & \frac{k_{GB2}}{\tau_2 I_6} & -\frac{\left(\frac{k_{GB2}}{\tau_2^2} + K_i\right)}{I_6} & 0 \\ 0 & 0 & 0 & 0 & \frac{k_{GB2}}{\tau_F \tau_2 I_6} & -\frac{\left(\frac{k_{GB2}}{\tau_2^2} + K_i\right)}{\tau_F I_6} & 0 \\ 0 & 0 & 0 & 0 & 0 & 0 & 0 \end{bmatrix}$$

$$A_{22} = \begin{bmatrix} -\frac{(c_{DMF} + c_1)}{I_1} & \frac{c_{DMF}}{I_1} & 0 & 0 & 0 & 0 & 0 \\ \frac{c_{DMF}}{I_2} & -\left(c_{DMF} + c_2 + \frac{c_{GB1}}{\tau_1^2}\right) & 0 & 0 & 0 & 0 & 0 \\ 0 & 0 & -\frac{(c_3 + c_{SA1})}{I_3} & \frac{c_{SA1}}{I_3} & 0 & 0 & 0 \\ 0 & 0 & \frac{c_{SA1}}{I_4} & -\frac{(c_{SA1} + c_4 + c_{SA2})}{I_4} & \frac{c_{SA2}}{I_4} & 0 & 0 \\ 0 & 0 & 0 & \frac{c_{SA2}}{I_5} & -\frac{(c_5 + c_{SA2})}{I_5} & 0 & 0 \\ 0 & 0 & 0 & 0 & 0 & -\frac{(c_6 + \frac{c_{GB2}}{\tau_2^2} + K_p)}{I_6} & 0 \\ 0 & 0 & 0 & 0 & 0 & -\frac{(c_6 + \frac{c_{GB2}}{\tau_2^2} + K_p)}{\tau_F I_6} & 0 \\ 0 & 0 & 0 & 0 & 0 & 0 & 0 \end{bmatrix}$$

$$A_{23} = \begin{bmatrix} \mathbf{O}_{5 \times 2} \\ -\frac{K_d}{I_6} & \frac{K_d}{I_6} \\ -\frac{(I_6 + K_d)}{\tau_F I_6} & \frac{K_d}{\tau_F I_6} \\ 0 & -\frac{1}{\tau_F} \end{bmatrix}$$

$$B_{CL} = \begin{bmatrix} \mathbf{O}_{6 \times 4} \\ \frac{1}{I_1} & 0 & 0 & 0 \\ \mathbf{O}_{4 \times 4} \\ 0 & \frac{K_i}{I_6} & \frac{K_p}{I_6} & 0 \\ 0 & \frac{K_i}{\tau_F I_6} & \frac{K_p}{\tau_F I_6} & 0 \\ 0 & 0 & 0 & \frac{1}{\tau_F} \end{bmatrix}$$

References

- 697 1. Schnabler, M., Stifter, C.: Model-Based Design Methods for the Development of Transmission
698 Control Systems. In: Conference Paper, SAE International, 0148-7191 (2014)
- 699 2. Castiglione, M., Stecklein, G., Senseney, R., Stark, D.: Development of Transmission
700 Hardware-in-the-Loop Test System. SAE Technical Paper, 2003-01-1027 (2003)
- 701 3. Bagalini, E., Violante, M.: Development of an automated test system for ECU software valida-
702 tion: An industrial experience. In: 15th Biennial Baltic Electronics Conference (BEC),
703 pp. 103–106, Tallinn, Estonia (2016)
- 704 4. Galvagno, E., Velardocchia, M., Vigliani, A., Tota, A.: Experimental Analysis and Model
705 Validation of a Dual Mass Flywheel for Passenger Cars. SAE Technical Paper, 2015-01-1121
706 (2015)
- 707 5. Hwang, T., Roh, J., Park, K., Hwang, J., Lee, K.H., Lee, K., Lee, S.-J., Kim, Y.-J.: Develop-
708 ment of HIL systems for active brake control systems. In: SICE-ICASE International Joint
709 Conference (2006)
- 710 6. Lee, S.J., Kim, Y.J.: Development of hardware-in-the-loop simulation system for testing
711 multiple ABS and TCS modules. *Int. J. Veh. Des.* **36**(1), 13–23 (2004)
- 712 7. Tota, A., Galvagno, E., Velardocchia, M., Vigliani, A.: Passenger car active braking system:
713 Model and experimental validation (Part I). *Proc. Inst. Mech. Eng. C J. Mech. Eng. Sci.* **232**(4),
714 585–594 (2018)
- 715 8. Tota, A., Galvagno, E., Velardocchia, M., Vigliani, A.: Passenger car active braking system:
716 Pressure control design and experimental results (part II). *Proc. Inst. Mech. Eng. C J. Mech.*
717 *Eng. Sci.* **232**(5), 786–798 (2018)
- 718 9. Galvagno, E., Tota, A., Vigliani, A., Velardocchia, M.: Pressure following strategy for conven-
719 tional braking control applied to a HIL test bench. *SAE Int. J. Passenger Cars-Mech. Syst.*
720 **10**(2017-01-2496), 721–727 (2017)
- 721 10. Lee, M.H., et al.: Development of a hardware in the loop simulation system for electric power
722 steering in vehicles. *Int. J. Automat. Technol.* **V12**, 733–744 (2011)
- 723 11. Galvagno, E., Tota, A., Velardocchia, M., Vigliani, A.: Enhancing Transmission NVH Perform-
724 ance through Powertrain Control Integration with Active Braking System. SAE Technical
725 Paper 2017-01-1778 (2017)
- 726 12. Galvagno, E., Velardocchia, M., Vigliani, A.: Torsional oscillations in automotive transmission:
727 Experimental analysis and modelling. *Shock Vibration* **2016** (2016)
- 728 13. Mendes, A., Meirelles, P.: Application of the hardware in-the-loop technique to an elastomeric
729 torsional vibration damper. *SAE Int. J. Engines* **6**(4), 2004–2014 (2013)
- 730 14. Bracco, G., Giorcelli, E., Mattiazzo, G., Orlando, V., Raffero, M.: Hardware-in-the-loop test
731 rig for the ISWEC wave energy system. *Mechatronics* **25**, 11–17 (2015)
- 732 15. Galvagno, E., Velardocchia, M., Vigliani, A.: Dynamic and kinematic model of a dual clutch
733 transmission. *Mech. Mach. Theory* **46**(6), 794–805 (2011)
- 734 16. Leonhard, W.: Control of Electrical Drives. Springer Science & Business Media (2001)
- 735 17. Welch, P.D.: The use of fast Fourier transform for the estimation of power spectra: a method
736 based on time averaging over short, modified periodograms. *IEEE Trans. Audio Electroacoust.*
737 **15**(2), 70–73 (1967)
- 738 18. Guercioni, G.R., Galvagno, E., Tota, A., Vigliani, A., Zhao, T.: Driveline Backlash and Half-
739 Shaft Torque Estimation for Electric Powertrains Control. SAE Technical Paper 2018-01-1345
740 (2018)
- 741 19. Osella, G., Cimmino, F., Galvagno, E., Vafidis, C., Velardocchia, M., Vigliani, A., Antonio,
742 T.O.T.A.: U.S. Patent No. 10946855. U.S. Patent and Trademark Office, Washington, DC
743 (2021)

Author Queries

Chapter 13

Query Refs.	Details Required	Author's response
AQ1	The closing parenthesis does not have a corresponding opening parenthesis in the caption of Fig. 4. Please insert the parenthesis in the appropriate position.	
AQ2	Caption of Figs. 10 and 14 seems to be identical. Please check and correct if necessary.	

UNCORRECTED PROOF

MARKED PROOF

Please correct and return this set

Please use the proof correction marks shown below for all alterations and corrections. If you wish to return your proof by fax you should ensure that all amendments are written clearly in dark ink and are made well within the page margins.

<i>Instruction to printer</i>	<i>Textual mark</i>	<i>Marginal mark</i>
Leave unchanged	... under matter to remain	Ⓟ
Insert in text the matter indicated in the margin	⋈	New matter followed by ⋈ or ⋈ [Ⓢ]
Delete	/ through single character, rule or underline or ┌───┐ through all characters to be deleted	Ⓞ or Ⓞ [Ⓢ]
Substitute character or substitute part of one or more word(s)	/ through letter or ┌───┐ through characters	new character / or new characters /
Change to italics	— under matter to be changed	↙
Change to capitals	≡ under matter to be changed	≡
Change to small capitals	≡ under matter to be changed	≡
Change to bold type	~ under matter to be changed	~
Change to bold italic	≈ under matter to be changed	≈
Change to lower case	Encircle matter to be changed	≡
Change italic to upright type	(As above)	⊕
Change bold to non-bold type	(As above)	⊖
Insert 'superior' character	/ through character or ⋈ where required	Υ or Υ under character e.g. Υ or Υ
Insert 'inferior' character	(As above)	⋈ over character e.g. ⋈
Insert full stop	(As above)	⊙
Insert comma	(As above)	,
Insert single quotation marks	(As above)	Υ or Υ and/or Υ or Υ
Insert double quotation marks	(As above)	Υ or Υ and/or Υ or Υ
Insert hyphen	(As above)	⊥
Start new paragraph	┌	┌
No new paragraph	┐	┐
Transpose	└┐	└┐
Close up	linking ○ characters	Ⓞ
Insert or substitute space between characters or words	/ through character or ⋈ where required	Υ
Reduce space between characters or words		↑